

**Toward efficient effective-one-body models for generic, nonplanar orbits**Rossella Gamba<sup>1,2,3</sup>, Danilo Chiaramello<sup>4</sup>, and Sayan Neogi<sup>3,5</sup><sup>1</sup>*Institute for Gravitation & the Cosmos, The Pennsylvania State University, University Park, Pennsylvania 16802, USA*<sup>2</sup>*Department of Physics, University of California, Berkeley, California 94720, USA*<sup>3</sup>*Theoretisch-Physikalisches Institut, Friedrich-Schiller-Universität Jena, 07743, Jena, Germany*<sup>4</sup>*INFN sezione di Torino, Torino, 10125, Italy*<sup>5</sup>*Indian Institute of Science Education and Research, Homi Bhabha Road, Pashan, Pune 411008, India*

(Received 29 April 2024; accepted 17 June 2024; published 16 July 2024)

Complete waveform models able to account for arbitrary nonplanar orbits represent a holy grail in current gravitational-wave astronomy. Here, we take a step toward this direction and present a simple yet efficient prescription to obtain the evolution of the spin vectors and of the orbital angular momentum along noncircularized orbits, that can be applied to any eccentric aligned-spins waveform model. The scheme employed is motivated by insights gained from the post-Newtonian (PN) regime. We investigate the phenomenology of the Euler angles characterizing the time-dependent rotation that connects the coprecessing frame to the inertial one, gauging the importance of noncircular terms in the evolution of the spins of a precessing binary. We demonstrate that such terms are largely negligible, irrespectively of the details of the orbit. Such insights are confirmed by studying the radiation-frame of a few eccentric, precessing numerical relativity (NR) simulations. Our investigations confirm that the usual “twisting” technique employed for quasispherical systems can be safely applied to noncircularized binaries. By then augmenting a state-of-the-art effective-one-body (EOB) model for noncircular planar orbits with the prescription discussed, we obtain an inspiral-merger-ringdown (IMR) model for eccentric, precessing binary black holes (BBHs). We validate the model in the quasispherical limit via mismatches and present one phasing comparison against a precessing, eccentric simulation from the RIT catalog.

DOI: [10.1103/PhysRevD.110.024031](https://doi.org/10.1103/PhysRevD.110.024031)**I. INTRODUCTION**

Ever since the first historic binary black hole (BBH) detection, the field of gravitational-wave (GW) astronomy has attracted much interest from the broader physics community. The wealth of information that can be garnered from the detection and analysis of compact binary coalescences (CBCs) has been proven time and time again [1–13], with the growth in the number of observed events being accompanied by detection of exceptional systems, each characterized by peculiar features such as very unequal masses [14,15], hints of spins precession [14,16,17], large total mass [18,19], the presence of one or more neutron stars (NSs) [2,20–22] and more. One such exceptional event, GW190521 [18,19], has been the center of attention for many groups, with a large number of possible astrophysical interpretations having been suggested [23–28]. Reference [23], in particular, suggested that GW190521 could be interpreted as the merger of two precessing black holes (BHs) coalescing along highly eccentric orbits. While successive studies have shown that the effects of precession and noncircularity on the detected signal are mostly degenerate for binaries with large total mass [25,29] and that prior

choices strongly affect the outcome of the analysis itself [30], it is nonetheless of paramount importance for the GW modeling community to be able to deliver models that can quickly and reliably generate waveforms for these kinds of binaries, thus covering a portion of the parameter space that has been up to now largely ignored. In fact, only by relying on complete models one can hope to fully understand the interplay between the two effects, and break the degeneracies discussed.

The history of the development of models containing precession is rather rich [31–36]. Most models now employ a “twist” technique [33–36], coupled with a way of obtaining the evolution of the so-called “coprecessing frame,” in which waveforms appear as if they were emitted by a quasialigned system [32,37]. While many nontrivial effects have just started to be properly understood and modeled, such as mode asymmetries or the merger-ringdown emission [38–40], it is safe to say that GW models of precessing binaries have reached a mature state [41–50], and they are now routinely employed in parameter estimation (PE) of GW data.

The inclusion of eccentricity, instead, is much more recent—and largely limited to the EOB [51–57] family of

models<sup>1</sup> that can rely on a Hamiltonian formulation of the dynamics not restricted to quasicircular or quasispherical systems [61,62]. Three main families of models exist: the SEOB<sub>NRE</sub> [63–65], TEOB<sub>ResumS-Dalì</sub> [66–69] and SEOB<sub>NRv4EHM</sub> [70] models. All differ in the way eccentricity is incorporated into the equations of motion—and in particular, in the radiation reaction driving the dissipative dynamics. While the SEOB<sub>NRE</sub> models include noncircular effects in the radiation reaction up to 2PN as an additive correction to the circular terms in the energy-balance equation, the TEOB<sub>ResumS-Dalì</sub> models employ a different strategy, and include the noncircular terms in the radiation reaction as a multiplicative Newtonian correction to the factorized EOB waveform. The SEOB<sub>NRv4EHM</sub> model does not include any explicit noncircular terms in the radiation reaction, which is driven by the circular terms only, but a posteriori includes 2PN order corrections in the computation of the waveform [71]. Comparisons of the validity of these approaches have been carried out in the test-mass limit [72], showing that for particles moving in Schwarzschild spacetimes the waveforms obtained with the TEOB<sub>ResumS-Dalì</sub> prescription are in excellent agreement with the exact numerical waveforms obtained solving the Regge-Wheeler-Zerilli (RWZ) and Teukolsky equations [73], and on average closer to the numerical results than the ones obtained by including explicit 2PN expressions.

The inclusion of both eccentricity and precession is a regime that is still mostly unexplored. A few studies have recently investigated the interplay between the two effects [74–79], but the considerations are typically (i) limited to purely PN (and at times Newtonian) arguments, (ii) based on orbit-averaged PN expressions, (iii) not immediately applicable to the full IMR regimes or (iv) not validated against full-fledged NR simulations. The lack of such simulations spanning a large number of orbital cycles and covering the parameter space of interest has so far limited the development of models for these systems. The only exception is the recent work of [80], who have extended the SEOB<sub>NRE</sub> model to include the evolution of the spins along noncircular orbits. In this work, the authors solve the full EOB equations, with a spherical (rather than planar) EOB Hamiltonian (borrowed from the SEOB<sub>NRv4</sub> model [81,82]), augmenting the spins equations of motions with explicit noncircular terms. While general, this approach is computationally expensive, and it is not clear whether it is truly necessary to solve the full spins equations of motion together with the EOB dynamics to obtain a faithful model for the precessing, eccentric regime.

In this paper, we present a simple yet efficient scheme to obtain waveforms from generic nonplanar orbits, that can be applied to any eccentric aligned-spins waveform model.

<sup>1</sup>Though note also the PN models of [58,59] and the non-spinning, eccentric surrogate of [60].

Section II is dedicated to a brief review of the PN equations of motion for noncircularized precessing binaries. Starting from the full 3PN equations of motion, we apply successive approximations to gauge the importance of noncircular terms in the evolutions of the spins. Section III tests the intuitions gained in the PN sector by identifying and inspecting the coprecessing (radiation) frame of a few chosen reference NR simulations [83]. We show that the evolution in this frame resembles that of an aligned-spin system, as expected. We also compare two simulations having same initial conditions but different eccentricities, corroborating the findings of Sec. II. Section IV presents the extension of the TEOB<sub>ResumS-Dalì</sub> model to include the evolution of the spins along noncircular orbits. Putting together the insights gained from the PN regime and the NR simulations, we show that the scheme employed is able to capture the main features of eccentric precessing waveforms. Section V is dedicated to the validation of the model in the quasicircular, precessing limit against the same simulations considered in [84]. We also present one phasing comparison against a precessing, eccentric simulation from the RIT catalog. Finally, Sec. VI summarizes the main results and discusses the implications of this work as well as avenues for future developments.

Throughout the paper we use geometrized units, setting  $G = c = 1$ . We denote the component masses of a binary system as  $m_1, m_2$ , and the total mass as  $M = m_1 + m_2$ ; the mass fractions are  $X_{1,2} = m_{1,2}/M$ , the mass ratio is  $q = m_1/m_2 \geq 1$ , and the symmetric mass ratio is  $\nu = q/(1+q)^2$ , with the reduced mass given by  $\mu = M\nu$ . The spin vectors are  $\mathbf{S}_1, \mathbf{S}_2$ , and they are related to the dimensionless spins  $\chi_{1,2}$  by  $\mathbf{S}_1 = m_1^2 \chi_1, \mathbf{S}_2 = m_2^2 \chi_2$ . The total spin is given by  $\mathbf{S} = \mathbf{S}_1 + \mathbf{S}_2$ , and the spin difference by  $\mathbf{\Sigma} = \mathbf{S}_2/X_2 - \mathbf{S}_1/X_1$ ; the effective spin variable is  $\chi_{\text{eff}} = X_1 \chi_{1,z} + X_2 \chi_{2,z}$ , while the orthogonal spin parameter is  $\chi_p = \max\{|\chi_{1,\perp}|, \frac{4+3q}{4q^2+3q} |\chi_{2,\perp}|\}$  [45].

## II. THE PN SANDBOX

While often unreliable from a quantitative point of view, PN theory is a powerful tool to gain qualitative insights on the dynamics of CBCs. In this section, we employ PN equations of motion to gauge the importance of noncircular terms in the evolution of the spins of a precessing binary, and more generically review the effects that nonquasicircular evolution has on the time-dependent rotation that connects the coprecessing frame to the inertial one. Our approach is often pedagogical, aiming to reinforce and extend the intuitions that have been acquired over the years during the development of quasispherical models for precessing binaries.

### A. Reference frames and equations of motion

Consider a BBH system with spins  $\mathbf{S}_1, \mathbf{S}_2$  and total mass  $M = m_1 + m_2$ , moving in a nonplanar orbit. Following the

notation employed in, e.g., [85,86], we describe the system in center of mass coordinates, and introduce the relative position and velocity vectors  $\mathbf{r}$ ,  $\mathbf{v}$ . We denote the unit vector of the relative position as  $\mathbf{n} = \mathbf{r}/r$ , and the unit vector pointing along the (Newtonian) orbital angular momentum  $\mathbf{L}$  as  $\boldsymbol{\ell} = \mathbf{n} \times \mathbf{v}/v$ . We choose an initial reference frame in which the  $z$ -axis is aligned with  $\boldsymbol{\ell}$ , and the  $x$ -axis is aligned with  $\mathbf{n}$ . The  $y$  axis is then chosen to complete a right-handed triad.

The equations of motion at 3PN order in modified harmonic coordinates have the form [85,86]:

$$\frac{d\mathbf{r}}{dt} = \mathbf{v}, \quad (1a)$$

$$\frac{d\mathbf{v}}{dt} = -\frac{Gm}{r^2}[(1 + \mathcal{A})\mathbf{n} + \mathcal{B}\mathbf{v}] + \frac{d\mathbf{v}_S}{dt} + \mathcal{O}\left(\frac{1}{c^7}\right), \quad (1b)$$

$$\frac{d\mathbf{S}}{dt} = (X_1\boldsymbol{\Omega}_1 + X_2\boldsymbol{\Omega}_2) \times \mathbf{S} + \nu(\boldsymbol{\Omega}_2 - \boldsymbol{\Omega}_1) \times \boldsymbol{\Sigma}, \quad (1c)$$

$$\frac{d\boldsymbol{\Sigma}}{dt} = (X_2\boldsymbol{\Omega}_1 + X_1\boldsymbol{\Omega}_2) \times \boldsymbol{\Sigma} + (\boldsymbol{\Omega}_2 - \boldsymbol{\Omega}_1) \times \mathbf{S}, \quad (1d)$$

with:

$$\boldsymbol{\Omega}_i = \boldsymbol{\ell} \left[ \frac{1}{c^2} \alpha_{1\text{PN}}^{(i)} + \frac{1}{c^4} \alpha_{2\text{PN}}^{(i)} + \frac{1}{c^6} \alpha_{3\text{PN}}^{(i)} + \mathcal{O}\left(\frac{1}{c^7}\right) \right]. \quad (2)$$

All coefficients listed in the equations above are functions of  $r$ ,  $\mathbf{v}$ ,  $\mathbf{S}$ ,  $\boldsymbol{\Sigma}$  and of the symmetric mass ratio  $\nu$  (or, alternatively, the component masses  $m_1$  and  $m_2$ ), and can be read from Eqs. (3.4a)–(3.7c) of [85] and Eqs. (355a)–(355d), (356a)–(356d) of [86]. Notably, the  $d\mathbf{v}_S/dt$  component of the acceleration contains a term parallel to  $\boldsymbol{\ell}$ , which is responsible for the precession of the orbital plane.

Following [49,84], we choose as our reference coprecessing frame  $\{\mathbf{x}', \mathbf{y}', \mathbf{z}'\}$  the one in which the  $\mathbf{z}'$  axis is aligned with the Newtonian angular momentum  $\boldsymbol{\ell}$  at all times. We parametrize the time-dependent rotation relating the  $\{\mathbf{x}, \mathbf{y}, \mathbf{z}\}$  and  $\{\mathbf{x}', \mathbf{y}', \mathbf{z}'\}$  frames as a sequence of three Euler angles  $\alpha(t)$ ,  $\beta(t)$ ,  $\gamma(t)$ :

$$\alpha = \arctan\left(\frac{\ell^y}{\ell^x}\right), \quad (3a)$$

$$\beta = \arccos(\ell^z). \quad (3b)$$

The third angle  $\gamma$  is obtained from  $\alpha$  and  $\beta$  by

$$\dot{\gamma} = \dot{\alpha} \cos \beta, \quad (4)$$

where the overdot denotes differentiation with respect to time. Note that, by construction, at the initial time  $\beta(0) = 0$ , while  $\alpha(0)$  and  $\gamma(0)$  are undefined according to the equations above. We resolve this ambiguity by

setting  $\alpha(0)$  according to Appendix A of [84] and  $\gamma(0) = \alpha(0)$ . This is not the only possible choice of coprecessing frame, as one could also specify the direction of the  $\mathbf{x}'$  axis at  $t = 0$  to be aligned with the initial  $\mathbf{n}$ .

We solve the equations of motion Eqs. (1) numerically, terminating the integration when the binary reaches the final peak of the orbital frequency  $\Omega = |\mathbf{v} \times \mathbf{r}|/r^2$ , surpasses a maximum threshold time or a minimum radial separation of  $r = 4M$ . As we will also be interested in the evolution of systems along quasicircular orbits, in order to perform direct comparisons with the results obtained in the general case, we implement an eccentricity-reduction scheme following [87,88].

We compute the dynamics of several systems with characteristics spanning the parameter space, varying the mass-ratio  $q \in [1, 9]$ , the component spins (with the initial values of the spin parameters  $\chi_{\text{eff}} \in [-0.9, 0.9]$  and  $\chi_p \in [0, 1]$ ), and the orbit geometry. We consider both bound orbits (defined by the initial eccentricity,  $e_0 \in [0.01, 0.9]$ , and dimensionless semilatus rectum,  $p_0$ ) and unbound configurations (scatterings, dynamical captures), where initial data is parametrized by the starting energy  $\hat{E}_0 = E_0/\mu$  and (orbital) angular momentum  $\hat{L}_0 = L_0/\mu$  (varied from just above the separatrix to high values), at an initial defined separation  $r_0 = 10000M$ .

We neglect, for simplicity, any terms in the PN expressions giving the initial velocities (see Appendix) that depend on the spins  $\mathbf{S}_1, \mathbf{S}_2$ . For unbound orbits, because of the very large initial separation, this leads to negligible differences between the given initial energy and angular momentum and the values recovered from the dynamics using the spin-dependent expressions ( $< 10^{-5}$  for the former,  $\lesssim 10^{-2}$  for the latter). For bound configurations, when the out-of-plane spin components are large and aligned with the orbital angular momentum, this approximation can result in more important deviations in the eccentricity and semilatus rectum as estimated from the dynamics (a value of  $e_0 = 0.9$  in input can result in a recovered initial eccentricity of  $\sim 0.93$ ). However, since eccentricity is not a gauge invariant parameter anyway, we accept this (usually very) slight incongruence and treat the nominal value of  $e_0$  as an approximate indicator of the degree of noncircularity in the orbit.

## B. Angular momentum vectors

We begin by reviewing the main results concerning the dynamical properties of eccentric, precessing binaries in the PN approximation, starting with a reminder of the effects of precession on the angular momentum vectors of the system.

If one neglects radiation reaction terms, the equations of motion for a generic precessing system admit two non-trivial conserved integrals in the center-of-mass frame: the energy and the total angular momentum vector, given by the sum of the orbital and spin contributions:

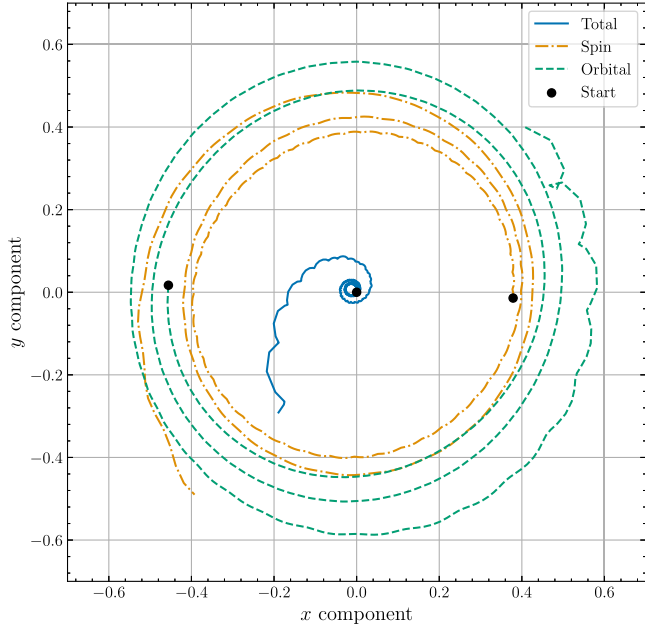


FIG. 1. Tracks of the evolving angular momentum (total and orbital) and (total) spin unit vectors, projected onto the plane perpendicular to the initial value  $\mathbf{J}_0$ . The mass ratio is  $q = 4$ , the initial eccentricity is  $e_0 = 0.7$ , the semilatus rectum  $p_0 = 30$ , and the dimensionless spins  $\chi_1 = (0, 0.8, 0.1)$ ,  $\chi_2 = (0.4, 0, 0.2)$ .

$$\mathbf{J} = \mathbf{L} + \mathbf{S}. \quad (5)$$

The evolution equations for the individual spins  $\mathbf{S}_1$ ,  $\mathbf{S}_2$  guarantee the conservation of their norm. Conversely, the modulus of the orbital angular momentum decays under radiation reaction, and with it  $\mathbf{J}$ . The resulting phenomenology for these vectors has been studied in detail in the literature (see, e.g., [31,89]), and our results are in line with the findings of such works irrespectively of the shape of the orbit. At 3PN order the total momentum  $\mathbf{J}$  is characterized by slowly decreasing magnitude and approximately conserved direction (outside of the last few orbits). In contrast, the orbital angular momentum  $\mathbf{L}$  and the total spin  $\mathbf{S}$  precess around  $\mathbf{J}_0$  on cones with increasing aperture. Figure 1, representative of all configurations studied,<sup>2</sup> shows the slowly outspiralling tracks of the unit vectors of  $\mathbf{J}$ ,  $\mathbf{L}$  and  $\mathbf{S}$ , projected onto a plane orthogonal to  $\mathbf{J}_0$ , for a system with mass ratio  $q = 4$ , large eccentricity ( $e_0 = 0.7$ ) and  $\chi_1 = (0, 0.8, 0.1)$ ,  $\chi_2 = (0.4, 0, 0.2)$ . The long tail in the track of  $\mathbf{J}$ , where conservation is clearly broken, corresponds to just the final cycles of the inspiral.

<sup>2</sup>With the exception of some rather extreme ones with  $q = 9$  and large, negative initial  $z$ -components in the spins. In this regime, the initial total spin and orbital angular momentum partially cancel out, but while the norm of  $\mathbf{S}$  does not change much during the inspiral,  $L$  decays due to radiation reaction, and this can lead to a peculiar *increase* in the norm of  $\mathbf{J}$ , as well as deviations from the phenomenology described in the text.

### C. Phenomenology of the Euler angles

We now move on to highlighting the relevant features of the evolution of the Euler angles, focusing on  $\beta$ , which is most directly tied to the precession of the orbital plane.

Figure 2 shows the evolution of the orbital frequency  $\Omega$  and of the Euler angle  $\beta$  for one exemplary system with mass ratio  $q = 4$ , spins  $\chi_1 = (0, 0.2, 0.1)$ ,  $\chi_2 = (0.4, 0, 0.2)$ , initial eccentricity  $e_0 = 0.1$  and semilatus rectum  $p_0 = 30$  (see Sec. II D for the meaning of the different curves). As is the case for all systems we consider,  $\beta$  starts from 0 (by construction), and over the course of the binary evolution undergoes a series of slow, but accelerating oscillations. It is immediately evident that the precession timescale characterizing these oscillations is much larger than the orbital period: the system completes  $\simeq 55$  orbits during the first  $\beta$  cycle in this example. This separation of timescales remains true for most of the configurations studied, as evidenced in Fig. 3, which shows two orbits with larger initial eccentricity ( $e_0 = 0.4$  and  $e_0 = 0.9$ ) but same initial spin vectors. Effects on  $\beta$  on the orbital timescale are present, at low eccentricities, exclusively in the form of small nutations around the overall, slower evolution. As eccentricity grows and the orbits part from quasicircularity, physical quantities such as the energy and the angular momentum vectors (and thus the Euler angles) undergo long stretches of stasis—rather than slow, secular changes—interspersed with short but intense bursts of activity, coinciding with periastron passages (see the bottom panel of Fig. 3).

While our focus has been on one single representative configuration of mass ratio and spins, the main characteristic features of the evolution of  $\beta$  do not change significantly when varying the initial conditions. Generally speaking, larger eccentricities and/or spin components in the direction of the orbital angular momentum lead to fewer oscillations, the first very stretched out (this is especially true when the  $z$ -components of the spins are antialigned with the initial  $\mathcal{L}$ ). The maximum value of  $\beta$  is only mildly influenced by the eccentricity, but depends strongly on the mass ratio and on the in-plane spin components (it is well known that larger  $q$  and  $\chi_p$  typically imply stronger precession).

The behavior that characterizes highly noncircular orbits is maximally evident for scatterings and captures, where each encounter is accompanied by a sudden change in the direction of  $\mathcal{L}$  and of the binary properties (energy, absolute value of the orbital angular momentum, directions of the spins) which then remain constant until the next encounter (if there is one). This is illustrated in Fig. 4, which shows the evolution of  $\beta$  for a series of scattering events with fixed  $q = 4$ , spins  $\chi_1 = (0, 0.8, 0.1)$ ,  $\chi_2 = (0.4, 0, 0.2)$ , initial energy  $\hat{E}_0 = 0.02$ , and  $\hat{L}_0$  growing from just above the threshold between bound and unbound orbits to  $\hat{L}_0 = 7$ . The shift in the orbital plane is more pronounced for systems with a smaller distance of closest approach (and  $\hat{L}_0$ ) as well as for systems with larger mass-ratio and/or

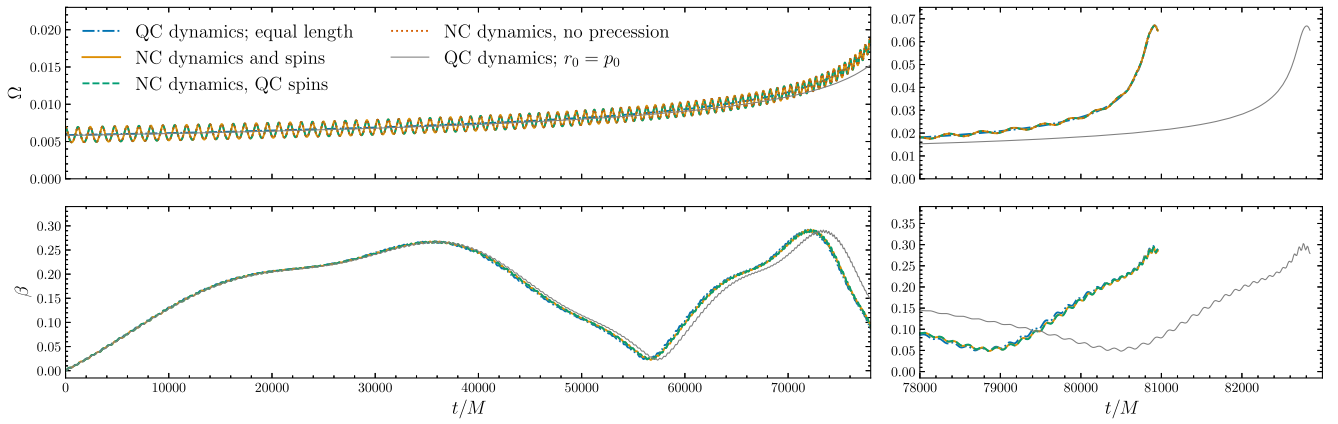


FIG. 2. Evolution of the orbital frequency  $\Omega$  (top) and the Euler angle  $\beta$  (bottom) for an orbit with  $q = 4$ , initial dimensionless spins  $\chi_1 = (0, 0.2, 0.1)$  and  $\chi_2 = (0.4, 0, 0.2)$ , initial eccentricity  $e_0 = 0.1$  and semilatus rectum  $p_0 = 30$ , using different prescriptions for the orbital and spin dynamics. Also shown are two wholly QC orbits: one with initial separation equal to  $p_0$ ; one with initial separation chosen so the length of the orbit is the same as the NC case. Notice how the QC evolution of  $\beta$  with suitable initial conditions almost exactly matches what is found in the NC orbits, with only small oscillating deviations on the orbital timescale.

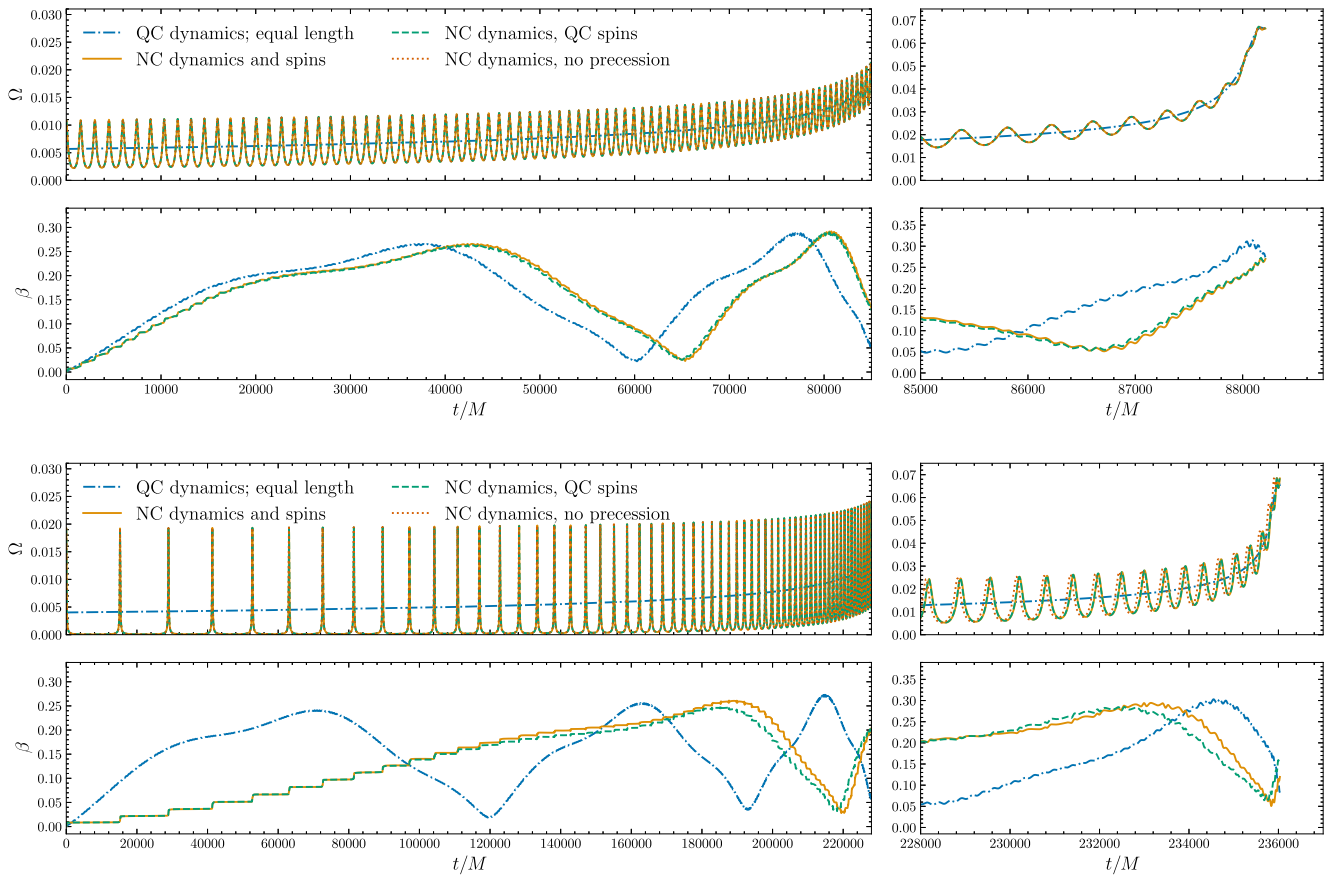


FIG. 3. Evolution of the orbital frequency  $\Omega$  and the Euler angle  $\beta$  using different prescriptions for the orbital and spins dynamics, for two eccentric orbits, both with  $q = 4$ , (initial)  $\chi_1 = (0, 0.2, 0.1)$  and  $\chi_2 = (0.4, 0, 0.2)$ :  $e_0 = 0.4$ ,  $p_0 = 30$  (top), and  $e_0 = 0.9$ ,  $p_0 = 30$  (bottom). In both cases an entirely QC orbit with same total duration is also shown. As the eccentricity increases, the slow variation of  $\beta$  on the precession timescale is no longer faithfully reproduced by the QC orbit; the difference between the orbit with full NC spin and orbital evolution and that with QC spin dynamics remains notably small even at high eccentricities.

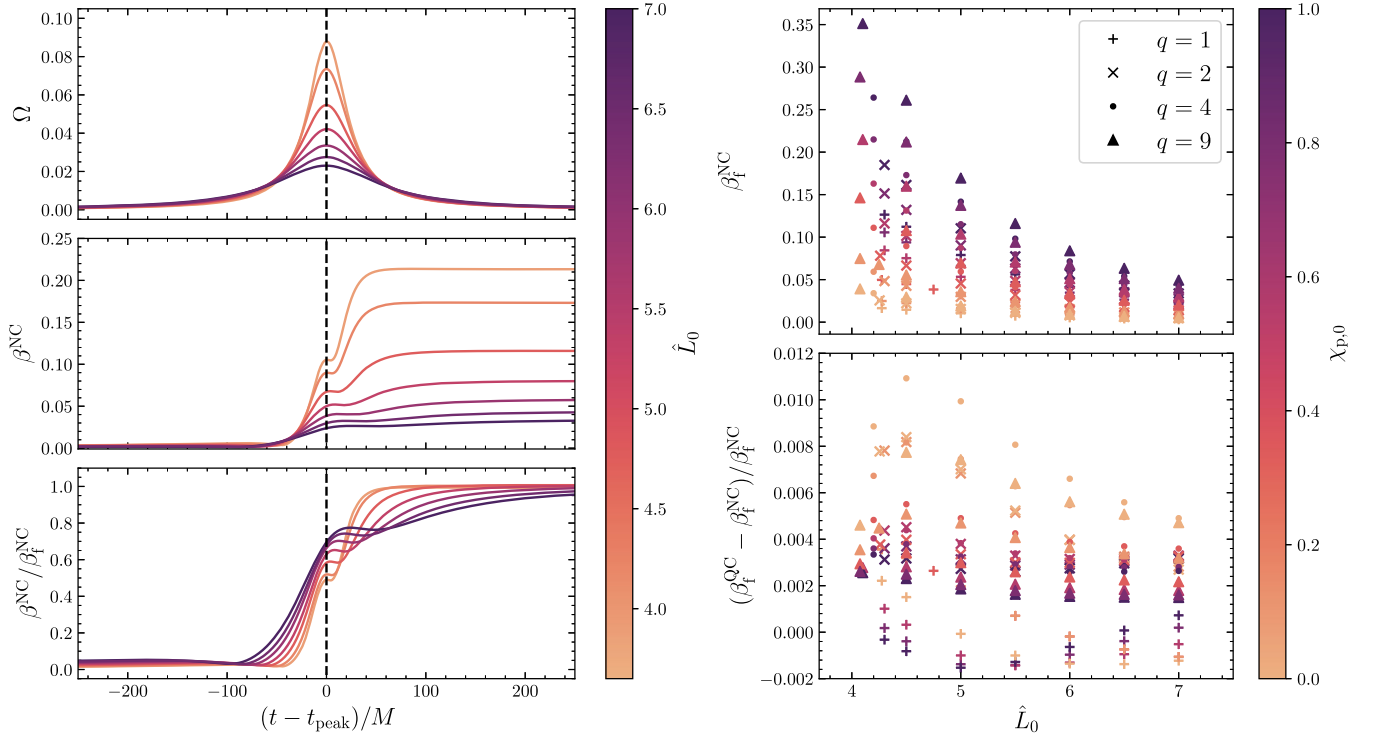


FIG. 4. On the left, the orbital frequency  $\Omega = |\mathbf{v} \times \mathbf{r}|/r^2$  (top) and Euler angle  $\beta$  (absolute, middle, and normalized by its asymptotic value, bottom) around the time of closest approach (corresponding to 0 on the horizontal axis, marked by a vertical dashed line) for a series of hyperbolic encounters with mass-ratio  $q = 4$ , initial spins  $\chi_1 = (0, 0.8, 0.1)$  and  $\chi_2 = (0.4, 0, 0.2)$  (so  $\chi_{p,0} = 0.8$ ), initial energy  $\hat{E}_0 = 0.02$  and varying initial orbital angular momentum  $\hat{L}_0$ . Smaller values of  $\hat{L}_0$  lead to closer encounters and to more pronounced and more sudden shifts in the orientation of the orbital plane. On the right: asymptotic value of  $\beta$  for scatterings with energy  $\hat{E}_0 = 0.02$ , mass-ratio  $q \in [1, 9]$ , varying  $\hat{L}_0$  and spins; comparison between  $\beta_f$  as calculated with the full noncircular model and neglecting noncircular terms in the spins evolution. The in-plane initial spin components are varied in norm (but keeping their directions fixed), while  $\chi_{1z,0} = 0.1$  and  $\chi_{2z,0} = 0.2$  for all cases, yielding  $\chi_{\text{eff},0} \in [0.11, 0.15]$ . After  $\hat{L}_0$ ,  $\beta_f$  is most strongly determined by the in-plane spin parameter, as can be expected; a secondary effect is a general increase in the asymptotic value of the Euler angle with the mass-ratio.

orthogonal spin parameter  $\chi_p^3$  (see Fig. 4). A curious feature is the inflection in the  $\beta$  curve at periastron: initially suspected to be a spurious effect due to the application of PN expansions in the strong field regime for the closest encounters, it appears to be a feature common to all cases considered, only becoming smoother and slower for larger  $\hat{L}_0$ .

#### D. The importance of noncircular terms

In order to better understand the importance of in-plane spins and noncircular terms in the system of Eqs. (1), we

<sup>3</sup>We mention in passing that  $\chi_p$  is known [90] to be an imperfect measure of the strength of spin precession. Configurations with initial in-plane spin components that are large in size, but oriented such that they cancel out in the total  $\mathbf{S}_\perp$ , have large  $\chi_p$ , but exhibit little to no precession if the mass ratio is close to 1. This is a consequence of the spin evolution equations in our PN study, and can also be seen in NR simulations as will be remarked later.

solve the equations of motion and compare the results obtained in four different scenarios:

- (i) with complete noncircular corrections fully accounted for in the evolution of the spins and the orbital dynamics (orange in Figs. 2 and 3);
- (ii) with noncircular corrections explicitly accounted for in  $d\mathbf{v}/dt$ , but not in  $\dot{\mathbf{S}}_1, \dot{\mathbf{S}}_2$  (green). This is done by setting  $\mathbf{\Omega}_{1,2}$  to its quasispherical reduction  $\mathbf{\Omega}_{1,2}^{\text{QC}}$  in the evolution equations of  $\dot{\mathbf{S}}_1, \dot{\mathbf{S}}_2$ , as given by Eq. (4.5) of Ref. [85]. Note that some generic-orbit effects are nonetheless present, as the parameter  $x = \Omega^{2/3}$  appearing in  $\mathbf{\Omega}_{1,2}^{\text{QC}}$  is inherited from the evolution of  $\mathbf{r}$  and  $\mathbf{v}$ ;
- (iii) with the dynamics of a quasispherical system (blue);
- (iv) with the dynamics of a planar noncircularized system (dotted red).

Figures 2 and 3 show the evolution of  $\Omega(t)$  (top) and  $\beta(t)$  (bottom) in the four scenarios above for the systems mentioned in the previous subsection. A few things can be immediately observed: (i) first, the impact of the

explicitly noncircular terms in  $\dot{\mathbf{S}}_1, \dot{\mathbf{S}}_2$  appears to be largely subdominant; (ii) second, the planar, noncircularized evolution of  $\Omega(t)$  provides a good approximation of the full evolution; (iii) third, the shape of  $\beta(t)$  (i.e., the number and height of  $\beta$  peaks) in the case of the quasispherical evolution matches that of the eccentric evolution, but it is “stretched” over time, similar to the evolution of  $\Omega(t)$ . In fact, if the initial conditions for the quasispherical evolution are slightly varied to generate orbital dynamics of approximately the same time length as the eccentric, precessing system, we find that  $\beta$  is almost perfectly overlaid with the target one. Points (i) and (ii) hold for every orbital and spin configuration considered, up to high eccentricity ( $e_0 = 0.9$ ) and in-plane spin components ( $\chi_p = 1.0$ ). The nonprecessing evolution at most accumulates a phase difference with respect to the precessing ones of one cycle in cases of very long, eccentric orbits.<sup>4</sup> The validity of point (iii) is more limited, as can be seen in the figures. Increasing the eccentricity ( $e_0 \gtrsim 0.2$ ), the evolutions of  $\beta$  as computed using quasicircular and noncircular dynamics become less and less comparable, with different characteristic time-scales, shapes, and numbers of cycles.

Our analysis thus seems to indicate that, so long as an “eccentric” prescription for  $\Omega(t)$  is employed, the quasicircular expressions for the spins may be sufficient to describe the precession of the orbital angular momentum up to large values of eccentricity  $e_0 \leq 0.9$ . Conversely, the worsening comparison between fully generic and quasicircular evolutions as the eccentricity grows suggests that the cumulative effect of the “bursts” observed at  $e_0 \geq 0.6$  cannot be fully captured by an orbit-averaging procedure. Indeed, Ref. [78] has shown that the multitimescale approach cannot be straightforwardly applied to highly eccentric systems, even at large separations. Nonetheless, it would be interesting to investigate whether it is possible to systematically map the noncircular dynamics to that of a circularized precessing system in the range  $e_0 \in [0.2, 0.6]$ , perhaps by focusing on matching orbit-averaged frequencies rather than the time-length of the orbits themselves.

### E. Scatterings

Given the importance of scatterings in the context of theoretical developments in GW physics [61,91–93], and in particular in the post-Minkowskian (PM) expansion [94–107], we dedicate a brief discussion to scatterings of nonplanar BBHs.

We consider a series of hyperbolic encounters with mass-ratios  $q \in [1, 9]$ , varying initial spins ( $\chi_{\text{eff}} \in [-0.9, 0.9]$  and  $\chi_p \in [0, 1]$ ), and initial energy  $\hat{E}_0 = 0.02$ . Increasing the initial orbital angular momentum  $\hat{L}_0$  from just above the

separatrix between bound and unbound orbits to high values, we evolve the system from an initial separation  $r_0 = 10\,000M$ , through the encounter, and out to the same final distance.

The outcome of a nonplanar encounter cannot be adequately described by a single scattering angle. We instead introduce two separate angles:  $\Phi = \varphi_f - \varphi_0 - \pi = \varphi_f - \pi$ , encoding the deflection in the original equatorial plane (perpendicular to  $\mathcal{L}_0$ ) and defined as the total variation in the azimuthal angular coordinate  $\varphi$  tied to the initial inertial frame; and  $\Theta = \theta_f - \theta_0 = \theta_f - \pi/2$ , describing the out-of-plane component and similarly defined in terms of the polar angle  $\theta$ .

Figure 5 displays the results for  $\Phi$  as a function of  $\hat{L}_0$ ,  $q$  and of the initial value of the spin parameter  $\chi_{\text{eff}}$ , for a collection of systems with  $\chi_{p,0} = 0.4$ . After the obvious dependence on  $\hat{L}_0$  (which determines the distance of closest approach and impact parameter), we see that  $\Phi$  is most correlated with the effective spin parameter  $\chi_{\text{eff}}$ : the scattering angle grows as  $\chi_{\text{eff}}$  decreases from positive (indicative of spin components initially aligned with the orbital angular momentum) to negative values ( $z$ -components initially anti-aligned with  $\mathbf{L}_0$ ). This effect is known, and can be intuitively

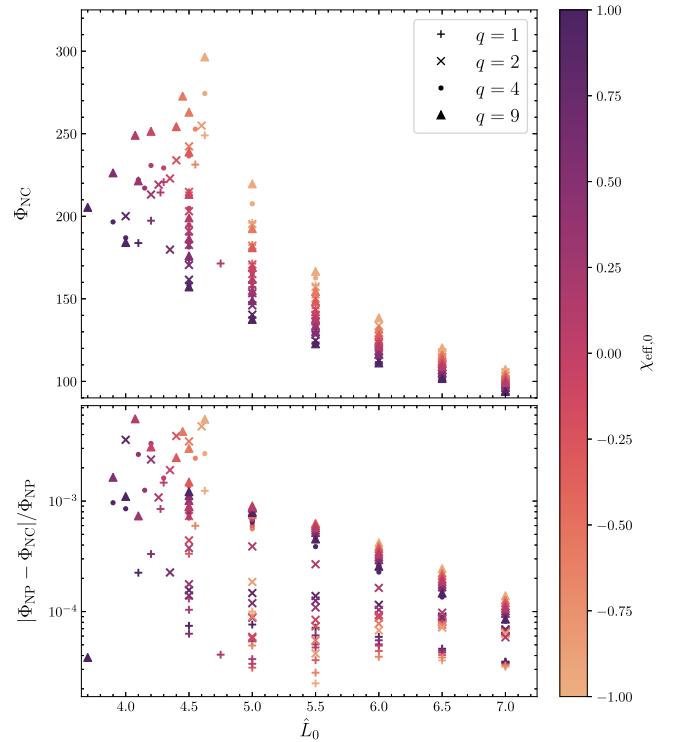


FIG. 5. Top panel: the azimuthal scattering angle  $\Phi_{\text{NC}}$ , in degrees, as a function of the initial orbital angular momentum  $\hat{L}_0$ ; color indicates the starting value of the effective spin parameter  $\chi_{\text{eff}}$ , while the marker corresponds to the mass-ratio  $q$ . The orthogonal spin parameter  $\chi_p$  is fixed at 0.4 for this plot. Bottom panel: relative differences between  $\Phi_{\text{NC}}$  and the scattering angle  $\Phi_{\text{NP}}$  computed neglecting spin precession.

<sup>4</sup>See also the bottom panel of Fig. 4, which highlights the small impact of the noncircular terms in  $\dot{\mathbf{S}}_1, \dot{\mathbf{S}}_2$  on the asymptotic value of the Euler angle  $\beta$  for scattering events.

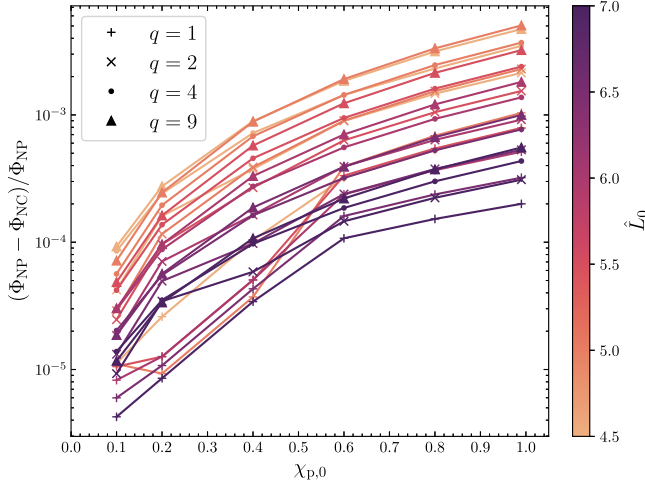


FIG. 6. Relative difference in the azimuthal scattering angle between fully NC and nonprecessing (NP) dynamics, for various mass ratios and initial angular momenta, as a function of the orthogonal spin parameter  $\chi_p$ ; the  $z$ -components of the initial dimensionless spins are fixed,  $\chi_{1,z} = 0.1, \chi_{2,z} = 0.2$ . Smaller  $\Phi$  signifies weaker interaction at closest approach; these results suggest that, everything else held equal, increasing in-plane spins has a slightly repulsive effect on the dynamics.

understood as a consequence of the spin-orbit interaction, which affects the effective radial potential [93]. Overlaid with this is a positive correlation with the mass-ratio, although this seems to be a somewhat sub-leading effect [note however that the two variables are not independent: recall that  $\chi_{\text{eff}} = X_1\chi_{1,z} + X_2\chi_{2,z} = (q\chi_{1,z} + \chi_{2,z})/(1+q)$ ].

The polar scattering angle  $\Theta$  is tied to the asymptotic value of the Euler angle  $\beta$ , and they display similar dependence on the system parameters. In fact,  $\Theta$  is geometrically bound to the interval  $[-\beta, \beta]$ ; its exact value (and in particular its sign, which corresponds to deviation either above or below the original equatorial plane) depends on the orientation of the in-plane spin components. In the configurations studied we found that  $|\Theta|$  remains close to 0 in most cases, with deviations from the original equatorial plane rarely exceeding  $5^\circ$ , and at most reaching  $15^\circ$  in cases of close encounters with high  $\chi_p$ .

The orthogonal spin variable  $\chi_p$ , encoding the strength of the precession effect, has a small impact on the orbital dynamics. Fixing the other parameters and increasing its magnitude from 0 to 1 leads to a decrease in  $\Phi$  of the order of  $\sim 1^\circ$ , or  $\lesssim 1\%$ , in most cases (see Fig. 6), with only the very closest encounters exhibiting stronger dependence on  $S_\perp$ ; this suggests that the in-plane spin components have a slightly repulsive effect in the binary interaction.

### III. THE STRONG FIELD REGIME

A comprehensive understanding of the strong field regime is pivotal for advancing the development of waveform models. Recently, simulations featuring both

eccentricity and precession have started to be made publicly available, with 7 new simulations from the MAYA catalog and 115 from the RIT catalog produced and shared over the past 2 years [83,108,109]. Unfortunately, most of these simulations exhibit a rather limited number of orbits before merger. For instance, the longest MAYA simulation available lasts only about  $1000M$  (approximately 5 orbits) before merger, while only 8 simulations from the RIT catalog surpass this duration. Furthermore, among these longer simulations, 3 feature a zero value for the in-plane component of the total spin  $\mathbf{S}_\perp = (S_x, S_y, 0)$ . This, combined with the fact that all of these systems are equal mass, implies that the orientation of the orbital angular momentum throughout the inspiral does not evolve.<sup>5</sup> Consequently, the majority of existing simulations are unsuitable for studying the inspiral phase, with the few exceptions being limited to equal mass configurations and lacking multiple resolutions.<sup>6</sup> In light of the limitations discussed, we concentrate on the two longest RIT simulations exhibiting clear precession effects, aiming to assess the validity of the physical intuition derived from the PN sector. Clearly, this focus does not constitute a comprehensive exploration of the strong field regime, but rather serves as an initial step in this direction.

Past works [33–36,111] have shown how it is possible to identify a coprecessing, noninertial frame from simulations of quasispherical inspiralling binaries in which the modulations induced by the spins precession appear decoupled from the orbital dynamics. Here, we extend the analysis to nonspherical orbits, showing that similar conclusions appear to hold also for eccentric systems. Given the lack of the full 3D information for the simulations that we consider, we extract the coprecessing frame following Appendix of [111] directly from the waveform multipoles  $h_{\ell m}$  or the Weyl scalar  $\psi_{\ell m}^A$ . We identify the preferred radiation axis  $\hat{\mathbf{V}}$  with the direction aligned with the principal direction of the  $\langle \mathcal{L}_{(a}\mathcal{L}_{b)} \rangle$  tensor [36,112]. After rotating the multipoles  $h_{\ell m}$  and  $\psi_{\ell m}^A$  to an inertial frame aligned with the initial direction of the orbital angular momentum  $\mathcal{L}$ , we compute the Euler angles  $\alpha, \beta, \gamma$  connecting the inertial “source” frame with the coprecessing frame (similar to what we did in the previous section), such that at each moment in time

$$\hat{\mathbf{V}} = (\cos \alpha \sin \beta, \sin \alpha \sin \beta, \cos \beta), \quad (6)$$

and the rotated multipoles read:

$$w_{\ell m}^R = \sum_{m'} D_{mm'}^\ell (R(\alpha, \beta, \gamma)^{-1}) w_{\ell m}, \quad (7)$$

<sup>5</sup>Notably, this is true for about 30% of the entirety of the RIT catalog of eccentric and precessing simulations.

<sup>6</sup>Such simulations can nonetheless be employed for the study of the merger-ringdown phase, see, e.g., [110].

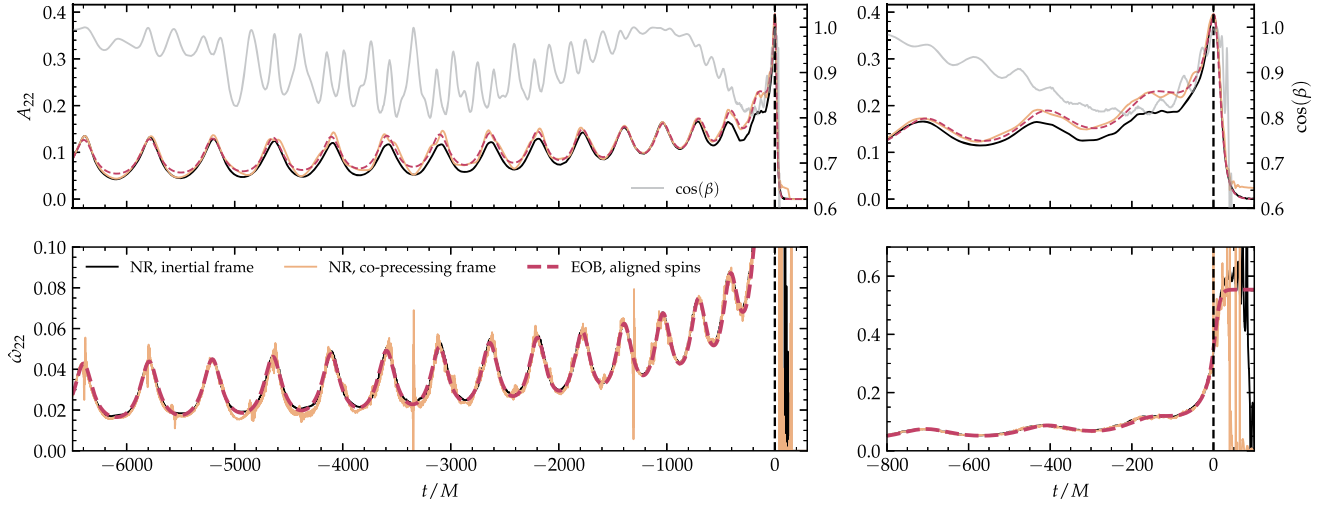


FIG. 7. Comparison between amplitude and frequency evolutions in the inertial and coprecessing frames. Aligned spins waveforms correctly capture the amplitude and frequency evolution of the coprecessing frame waveforms. Clear modulations, mimicking the oscillations in  $\beta$ , are visible in the inertial frame due to the precession of the spins.

where  $w_{\ell m}^R = \{h_{\ell m}^R, \psi_{\ell m}^{4,R}\}$  and  $R$  denotes the rotation matrix associated with the Euler angles.

An example of  $h_{22}$  in the radiation and inertial frames can be inspected from Fig. 7 for the RIT:eBBH:1632 simulation. This simulation is characterized by the following intrinsic parameters:  $q = 1$ ,  $\chi_1 = (-0.7, 0, 0)$ ,  $\chi_2 = (-0.7, 0, 0)$  and initial eccentricity of 0.28 at an initial radial separation of  $r_0 \sim 25M$ . While subtle, the modulations due to precession in the inertial frame are clearly visible, especially in the mode's amplitude close to the time of merger and around  $3000M$  before this time.

Predictably, these moments correspond to the times at which the  $\beta$  angle is significantly different from zero, as can be seen from the top panel of the same figure. The frequency evolution of the  $(2, 2)$  mode, shown in the bottom panel, instead does not appear to be significantly affected by the precession of the spins, although large numerical error seems to be present. We then compare the amplitude and frequency evolutions of the waveform in these two frames with those obtained with the aligned-spin EOB model of [113], that will be discussed in more detail in later sections (see Sec. IV). We fix the intrinsic

RIT:eBBH:1632

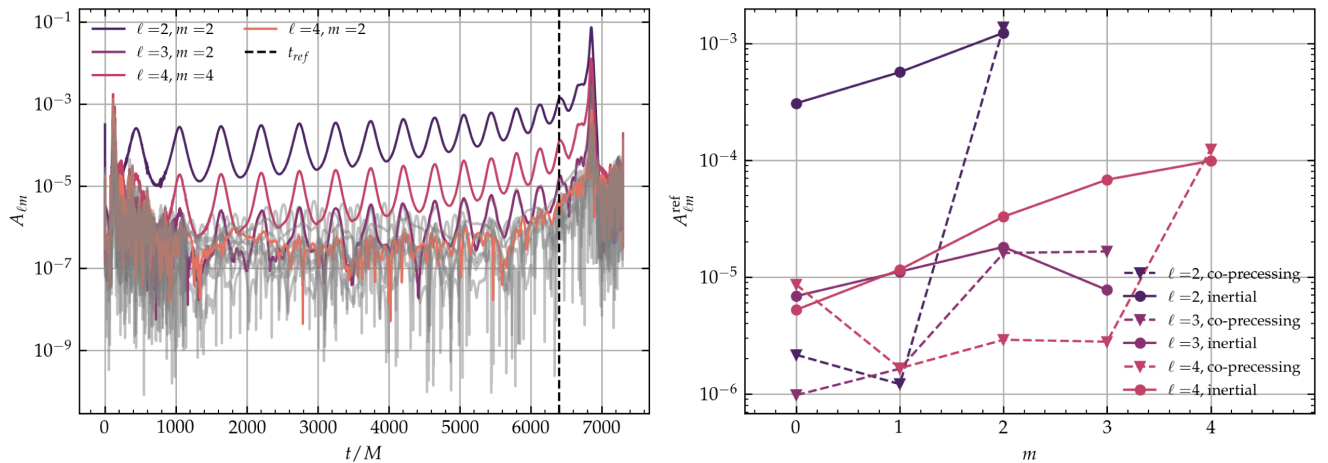


FIG. 8. Evolution (left) and hierarchy (right) of  $\psi_{\ell m}^4$  modes for the RIT:eBBH:1632 simulation in the coprecessing and inertial frames. In the right panel, the amplitudes are evaluated at a reference time  $t_{\text{ref}}$  corresponding to the last periastron before merger, and shown as a function of  $m$  for a fixed value of  $\ell$ , up to  $\ell = 4$ . The modes with  $\ell > 2$ , with the exception of the  $(4, 4)$  mode, are affected by large numerical noise. Nonetheless, it is possible to appreciate that odd- $m$  modes in the coprecessing frame have typically lower average amplitude than the even- $m$  ones. This is expected, as the system considered is an equal mass binary.

parameters of the EOB model (mass ratio,  $z$ -component of the spins) to the initial values specified in the simulation's metadata, and choose initial values of orbit-averaged frequency, eccentricity and true anomaly such that the frequency peaks of the EOB waveform approximately match the ones of the NR waveform, and the lengths of the waveforms are comparable. Remarkably, the amplitude and frequency evolutions thus obtained match the ones observed in the coprecessing frame, indicating that the simplification upon which the twisting procedure applied in the quasicircular scenario is based holds also for eccentric systems.

Additional evidence that this is the case is provided by an inspection of the hierarchy of the waveform modes in the coprecessing and inertial frames. We show the results of this analysis in Fig. 8, where we display the evolution of the amplitudes of the  $\psi_{\ell m}^A$  modes during the inspiral (left panel), and their values at a reference point corresponding to the last periastron before merger (right panel). The latter are shown as a function of  $m$  for a fixed value of  $\ell$ , up to  $\ell = 4$ . In spite of the large numerical noise that affects the modes with  $\ell > 2$ , with the exception of the (4, 4) mode, it is nonetheless possible to appreciate that odd- $m$  modes in the coprecessing frame have typically lower average amplitude than the even- $m$  ones, as one would expect from an aligned-spin, equal mass simulation. This is especially visible for  $m = 1$  modes, whose amplitudes in the inertial frame are at least one order of magnitude larger than the ones in the coprecessing frame. While not the case for the system considered, we remind the reader that for more eccentric simulations ( $e \geq 0.8$ ), e.g., RIT:eBBH:1199 or RIT:eBBH:1132, the amplitude at merger of the (2, 0) mode is not negligible, but rather can be comparable to that of the

(2, 2) mode, or larger. This is in contrast to the quasicircular case, where the (2, 0) mode is approximately zero up until merger.

We conclude this section by observing that the Euler angles extracted from the simulation considered above are morphologically very similar to the ones computed from the RIT:eBBH:1631 data. The latter is characterized by the same intrinsic parameters as RIT:eBBH:1632, but by a smaller initial eccentricity of  $e \sim 0.19$  at approximately the same initial separation. This fact is demonstrated in Fig. 9, which shows the evolution of the components  $\hat{V}_x, \hat{V}_y, \hat{V}_z$  of the radiation frame vector  $\hat{\mathbf{V}}$  for the two simulations. The two evolutions are clearly characterized by different timescales (represented in the two  $x$ -axes of the plots), due to their different orbital eccentricity, but—once appropriately rescaled—appear rather close to one another. This fact is consistent with the studies performed in the previous section, and suggests that the Euler angles are in general weakly affected by the eccentricity of the orbit even in the strong field regime, up to merger.

#### IV. AN EFFICIENT DESCRIPTION OF ECCENTRICITY AND PRECESSION

After discussing the phenomenology of eccentric, precessing dynamics in both the PN and NR regimes, it is finally time to move to the construction of a model that is able to quantitatively capture the waveforms emitted by such systems, wielding the insights obtained through our previous studies. In particular, we will first review the main features of the EOB model employed to obtain the coprecessing waveforms, recall the simplifications that are made to obtain the quasispherical, precessing waveforms, and finally discuss the generalization of the spin dynamics of Refs. [49,84] to the noncircular case.

##### A. Coprecessing waveform model

The baseline model that we employ for the description of the coprecessing motion is the `TEOBResumS-Dalì` approximant of [67,113]. Within the framework of this model, the dynamics of the system is obtained from the EOB equations of motion implied by the Hamiltonian  $H_{\text{EOB}}$ . Assuming planar orbits, the latter is a function of the variables  $\{r, p_{r*}, p_\varphi, \mathbf{S}, \mathbf{S}_*\}$ , where  $r$  is the radial separation,  $p_{r*}, p_\varphi$  are the conjugate momenta to  $r_* = \int dr(A/B)^{-1/2}$ ,  $\varphi$ , with  $A, B$  being the EOB potentials, and  $\hat{\mathbf{S}} = (\mathbf{S}_1 + \mathbf{S}_2)/M^2$ ,  $\hat{\mathbf{S}}_* = (1/q\mathbf{S}_1 + q\mathbf{S}_2)/M^2$  are dimensionless combinations of the spins of the binary components. Explicitly, the EOB Hamiltonian is given by

$$\hat{H}^{\text{EOB}} = \frac{1}{\nu} \sqrt{1 + 2\nu(\hat{H}_{\text{eff}} - 1)} \quad (8)$$

where  $\hat{H}_{\text{eff}}$  is the effective Hamiltonian

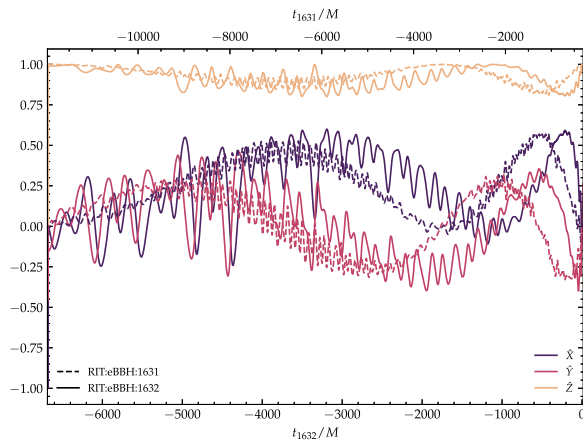


FIG. 9. Comparison of the evolution of the radiation frame components  $\hat{V}_x, \hat{V}_y, \hat{V}_z$  of the  $\hat{\mathbf{V}}$  vector for the RIT:eBBH:1631 and RIT:eBBH:1632 simulations. The two simulations are characterized by the same intrinsic parameters, but by different initial eccentricities. The Euler angles are weakly affected by the eccentricity of the orbit, and are morphologically very similar in the two cases.

$$\hat{H}_{\text{eff}} = \sqrt{A(1 + p_\varphi^2 u_c^2 + Q) + p_{r^*}^2 + p_\varphi(G_S \hat{S} + G_{S^*} \hat{S}^*)}. \quad (9)$$

The EOB potentials  $A$ ,  $D$ ,  $Q$  are considered at local 5PN order [114], and resummed according to [68]. The gyro-gravitomagnetic functions  $G_S, G_{S^*}$ , which encode spin-orbit contributions, are instead taken at next-to-next-to-leading order (NNLO) [68,115], and inverse-resummed following usual EOB prescriptions [116]. Even in spin effects are accounted for by the centrifugal radius  $u_c$  [68,115], here considered up to next-to-leading order (NLO). Two NR-informed parameters,  $a_6$  and  $c_3$ , complete the conservative sector of the model and ensure robustness up to merger [113]. The motion of the system is then obtained by evolving the set of equations

$$\frac{dr}{dt} = \left(\frac{A}{B}\right)^{1/2} \frac{\partial \hat{H}^{\text{EOB}}}{\partial p_{r^*}}(r, p_{r^*}, p_\varphi) \quad (10a)$$

$$\frac{d\varphi}{dt} = \Omega = \frac{\partial \hat{H}^{\text{EOB}}}{\partial p_\varphi}(r, p_{r^*}, p_\varphi) \quad (10b)$$

$$\frac{dp_{r^*}}{dt} = \left(\frac{A}{B}\right)^{1/2} \left(-\frac{\partial \hat{H}^{\text{EOB}}}{\partial r}(r, p_{r^*}, p_\varphi) + \hat{\mathcal{F}}_r\right), \quad (10c)$$

$$\frac{dp_\varphi}{dt} = \hat{\mathcal{F}}_\varphi(r, p_{r^*}, p_\varphi) \quad (10d)$$

which replace the equivalent equations for the PN dynamics given by Eq. (1). The radial and azimuthal back-reaction forces  $\hat{\mathcal{F}}_\varphi$  and  $\hat{\mathcal{F}}_r$  are computed from the EOB waveform, and contain noncircular corrections via the leading order Newtonian prefactor  $\hat{f}_\varphi^{\text{nc}}$  [66]:

$$\hat{\mathcal{F}}_\varphi^{\text{EOB}} = -\frac{32}{5} \nu r_\omega^A \Omega^5 \hat{f}_\varphi^{\text{nc}} \hat{f}(\Omega). \quad (11)$$

The model was recently shown to be more than 99% faithful to both quasicircular and eccentric [113] NR simulations up to merger and beyond. The model has also been tested against 15 nonspinning scattering simulations from Refs. [61,91], 21 spinning scattering systems from Ref. [93], multiple dynamical captures simulations from Refs. [28,117] as well as a large number of test-mass Regge-Wheeler-Zerilli and Teukolsky waveforms [73,118]. More details and an in-depth discussion of the model can be found in Ref. [113].

## B. Quasispherical precessing orbits

Most state-of-the-art EOB models for precessing, quasispherical BBHs do not directly solve a fully coupled PN system of ordinary differential equations (ODEs) describing the spins and orbital dynamics, such as Eq. (1). Instead,

they employ a scheme which relies on a split between precessing and orbital evolutions, the former typically considered in PN form, the latter from the planar, resummed EOB dynamics. This scheme, inspired by phenomenological models, was first introduced in the context of the EOB framework by Ref. [49] and then further improved upon and refined in Refs. [50,84]. The ODEs system considered by the TEOBResumS family for the spins evolution is of the form

$$\dot{\mathbf{S}}_1 = f_1(\Omega, \eta, \boldsymbol{\ell}, \mathbf{S}_1, \mathbf{S}_2), \quad (12a)$$

$$\dot{\mathbf{S}}_2 = f_2(\Omega, \eta, \boldsymbol{\ell}, \mathbf{S}_1, \mathbf{S}_2), \quad (12b)$$

$$\dot{\boldsymbol{\ell}} = f_L(\Omega, \eta, \dot{\mathbf{S}}_1, \dot{\mathbf{S}}_2), \quad (12c)$$

$$\dot{\Omega} = \dot{\Omega}_{\text{PN}}(\Omega, \eta, \boldsymbol{\ell}, \mathbf{S}_1, \mathbf{S}_2), \quad (12d)$$

where  $f_1, f_2, f_L$  and  $\dot{\Omega}_{\text{PN}}$  can be read from [49].

Critically, independently evolving the spins and the orbital dynamics allows for a significant reduction in the computational cost of the model, which—in the quasicircular limit—can rely on analytical acceleration techniques such as the postadiabatic (PA) [119] and stationary-phase approximation (SPA) [120] to obtain the waveform. The matching between the two evolutions of Eqs. (10) and (12d) represents the most delicate point in the scheme, and is typically performed by interpolating the Euler angles  $\alpha, \beta, \gamma$  obtained from the precessing dynamics to the orbital (PN) frequency, and then identifying  $\Omega_{\text{PN}}$  with the orbital EOB frequency  $\dot{\varphi} = \partial \hat{H}^{\text{EOB}} / \partial p_\varphi$  or the waveform frequency  $\sim \omega_{22}/2$  to obtain the map to EOB time; see Sec. II C of Ref. [84] for more details. Models based on this scheme were shown to be faithful to a large number of precessing, quasispherical NR simulations from the Simulating eXtreme Spacetimes (SXS) catalog. The TEOBResumS-GIOTTO model in its first IMR precessing iteration, in particular, was validated against 99 NR simulations in the `1vcnr` catalog, and 20 additional simulations with mass ratios  $q \leq 4$  and  $\chi_p \leq 0.49$  with more than 70 cycles. Its median unfaithfulness against these sets was found to be  $7 \times 10^{-3}$  and  $5 \times 10^{-3}$  respectively, for an inclination  $\iota = \pi/3$  [84].

## C. Generalized spins dynamics

We now aim to extend the procedure summarized in the previous section to noncircular orbits. There are a few obvious ways to do so. We list them below in order of growing complexity:

- (i) Use the evolution of  $\Omega(t)$  given by TEOBResumS-Dalì in place of  $\dot{\Omega}_{\text{PN}}$ . This immediately allows for the inclusion of eccentricity-related effects and—since no interpolation or orbit averaging is

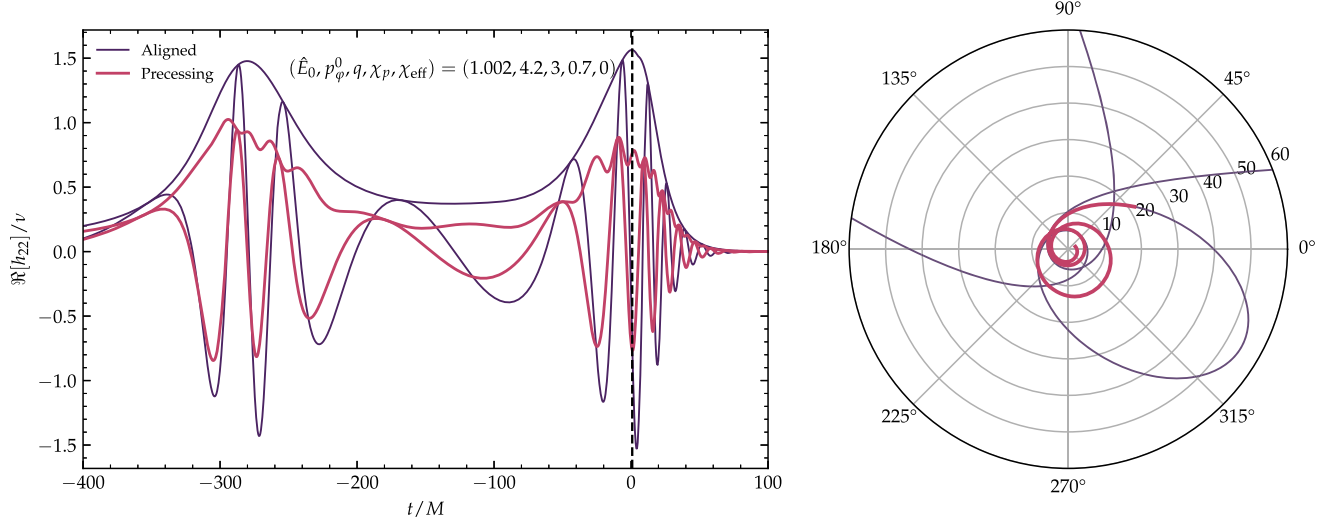


FIG. 10. Quadrupolar waveform mode (left) and coprecessing orbit (right) for a dynamically captured system with mass ratio  $q = 3$ , spins  $\chi_1 = (0.7, 0, 0)$ ,  $\chi_2 = (0, 0, 0)$  and initial energy, angular momentum and EOB radial separation 1.002, 4.2 and 10000. We compare the precessing waveform to its aligned spin counterpart. The portion of the waveform shown in the left panel is highlighted in the orbit plot on the right with a dark red line. Noticeable modulations, due to the mixing between  $\ell = 2$  coprecessing modes, can be observed at each periastron passage and at the time of merger.

required—this strategy can be applied to all kinds of systems, including scatterings and captures. While no contributions of (explicit) “noncircularity” to  $\dot{\mathbf{S}}_1, \dot{\mathbf{S}}_2, \dot{\mathcal{L}}$  are considered, the results of Sec. II indicate that this does not represent a significant issue for eccentric systems. A bigger drawback is represented by the fact that the evolution of the spins requires the EOB dynamics to be evolved first, making it not straightforward to account for time-varying contributions to the orbital dynamics.

- (ii) Solve the quasicircular PN spin precessing equations and use them to obtain the Euler angles  $\alpha, \beta, \gamma$ . Interpolate the angles in the frequency domain, and map them to an orbit-averaged EOB (orbital) frequency (see, e.g., Sec. IID of [121]). This method has the advantage of allowing for the inclusion of time-varying contributions to the orbital dynamics, so long as one is able to compute—at each moment of the EOB dynamics evolution—an orbit-averaged frequency. Once more, thanks to the difference in the orbital and precession timescales, this simple technique is expected to work well for mildly eccentric binaries. It however cannot be applied to, e.g., scatterings or captures, and neglects all contributions of “noncircularity” to the spins dynamics.
- (iii) Solve the quasicircular PN spin precessing equations together with the generic EOB orbital dynamics. This method allows for the inclusion of time-varying spins contributions while retaining both the ability to account for generic orbital configurations beyond eccentric systems and the theoretical simplifications that come with employing a coprecessing orbital

dynamics description.<sup>7</sup> Its main limitation is represented by its increased computational cost with respect to the previous options, as it requires the solution of a coupled system of 12 ODEs.

- (iv) Solve the spins dynamics equations of [76,78,122], together with orbital dynamics explicitly parametrized in terms of (quasi-Keplerian) eccentricity, anomaly and orbit-averaged frequency. This method extends the previous one by including the effects of eccentricity on the spins dynamics, while still allowing for the inclusion of time-varying contributions to the orbital dynamics and being applicable to larger values of eccentricity. However, it retains the limitation of not being applicable to all kinds of systems, as it assumes a parametrization of the orbital dynamics where eccentricity is explicitly present.

For the time being, we choose to adopt the first strategy, as it is the simplest to implement and—at the same time—represents a good compromise between accuracy, computational cost and generality.

The chosen method is then implemented following these steps:

- (i) We first obtain the evolution of the system in the coprecessing frame, assuming that waveforms can be well approximated by those given by the `TEOBResumS-Dalì` aligned-spins model.

<sup>7</sup>By this we mean that the EOB Hamiltonian and radiation reaction forces employed are those used for planar orbits, which are better studied than their nonplanar counterparts.

- (ii) From the coprecessing frame EOB dynamics we extract the orbital frequency evolution  $\Omega(t)$  (or, alternatively, the waveform frequency evolution  $\omega(t) \sim \omega_{22}(t)/2^8$ ).
- (iii) We employ this EOB evolution of the frequency to drive the evolution of the spins in the coprecessing frame, utilizing the orbit-averaged PN expressions for  $\hat{\mathbf{S}}_1, \hat{\mathbf{S}}_2, \hat{\mathcal{L}}$  of [49].
- (iv) With the evolution of the spins at hand, we compute the Euler angles and rotate the coprecessing waveforms to the inertial frame as described in, e.g., [49,84].
- (v) We extend  $\alpha, \beta, \gamma$  beyond merger by fixing them to their merger values.

This scheme is computationally cheaper than a full evolution of the 3D EOB dynamics, with no additional ODEs to solve and no need for a new Hamiltonian with respect to the quasispherical case. It largely relies on the assumption that noncircular terms in the spins dynamics are negligible and that the evolution of the orbital dynamics is not strongly affected by time-varying spins contributions. Both assumptions were shown to be approximately true in Sec. II, and can be expected to hold up even close to merger, where the system circularizes. The twisting procedure, too, does not appear to require modifications with respect to the quasicircular case, as was empirically demonstrated in Sec. III. Beyond the mildly eccentric case, this scheme can be applied also to unbound systems, scatterings and captures (see Fig. 10), although the validity of the orbit-averaged expressions for the spins dynamics is uncertain in these regimes.

## V. VALIDATION

We conclude the results presented in this work by validating the model in the quasicircular, precessing limit, comparing its performance to that of the TEOBResumS-GIOTTO model of Ref. [84]. We then move on to compare the model to one mildly eccentric, precessing waveform from the RIT database. This comparison is performed in the time domain, focusing mainly on the (2,2) and (2,1) modes. Given the lack of availability of multiple resolutions, as well as the fact that most other eccentric and precessing waveforms are either not very eccentric or not very long, we leave a more in-depth validation of the model in this regime to future works, where we will also present new eccentric and precessing simulations of BBHs [123].

### A. Quasicircular, precessing limit

Following the same procedure detailed in Sec. III of Ref. [84], we compare the model presented in this work to 99 NR simulations from the `lvcnr` catalog, spanning mass

ratios  $q \leq 6$ ,  $\chi_p \leq 0.89$  and  $\chi_{\text{eff}} \in [-0.45, 0.65]$ , and 21 “long” simulations of BBHs with mass ratios  $q \leq 4$  and spins  $\chi_p \leq 0.49$  and  $\chi_{\text{eff}} \in [-0.2, 0.3]$ . We quantify the goodness of our model in terms of the sky-maximized unfaithfulness [47,124,125], which is defined as:

$$\bar{\mathcal{F}}_{\text{SM}} = 1 - \max_{t_0^h, \varphi_0^h, \kappa^h, \xi_0} \frac{(s, h)}{\sqrt{(s, s)(h, h)}}, \quad (13)$$

where  $s$  is the target (NR) waveform,  $h$  is the model waveform and the maximization is performed over reference time  $t_0^h$ , reference phase  $\varphi_0^h$ , effective polarization angle  $\kappa^h$  and over an initial rotation of the in-plane spins  $\xi_0$ . This quantity is then signal-to-noise ratio (SNR) weighted, and averaged over the sky, the polarization and the initial phase of

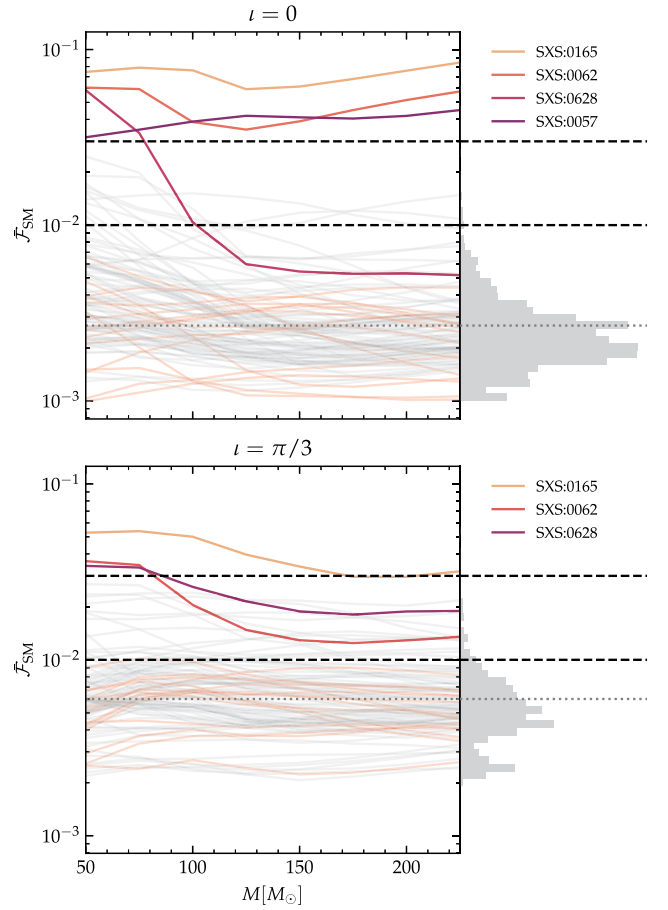


FIG. 11. Mismatches of the model for the 99 NR simulations of the `lvcnr` catalog (gray) and the 20 “long” simulations (red) discussed in the text, for different total masses and two different fixed values of inclination:  $i = 0$  (top) and  $i = \pi/3$  (bottom). We highlight with colored lines all simulations which at any total mass value cross the 3% threshold. Between inclinations, the more problematic simulations are the same, but the overall performance of the model worsens for increasing  $i$ , as expected. We find median unfaithfulnesses of  $0.003^{+0.009}_{-0.001}$  and  $0.006^{+0.010}_{-0.003}$  for  $i = 0$  and  $i = \pi/3$  respectively.

<sup>8</sup>Notably, this relation is only approximately valid for low eccentricities.

the target waveform: we choose four different values for the effective polarization,  $\kappa^s = \{0, \pi/4, \pi/2, 3\pi/4\}$ , and six values for the target reference phase,  $\varphi_0^s = \{0, 2\pi/5, 4\pi/5, 6\pi/5, 8\pi/5\}$ , to average over. We fix the power spectral density of the detector to the zero-detuned high-power advanced LIGO design sensitivity [126], and compute mismatches from 20 to 2048 Hz using the  $(\ell, |m|) = (2, 2), (2, 1), (3, 3), (4, 4)$  modes.

Results are displayed in Fig. 11, where we show the mismatches of the model for the simulations considered as a function of the total mass of the system for two target inclinations  $\iota = 0$  and  $\iota = \pi/3$ . Global distributions of the mismatches are also shown as histograms in the right panel of the same figure. We find that for the majority of the simulations the model is able to maintain an unfaithfulness below 3%, with the notable exceptions of the SXS:BBH:0165, SXS:BBH:0062, SXS:BBH:0628 and SXS:BBH:0057 simulations. These systems are characterized by either very asymmetric mass ratios ( $q \geq 5$ ), strong precession ( $\chi_p > 0.7$ ) or both, and are known to be challenging for GW models in general (see Table 2 of [127]). The global unfaithfulness found for the set considered with  $\iota = 0$  is  $0.003^{+0.009}_{-0.001}$ , where we employ the standard notation of quoting the median and the 90% confidence interval of the distribution. As inclination is increased from  $\iota = 0$  to  $\iota = \pi/3$ , the model becomes overall less faithful, especially for the merger-ringdown portion of the waveform. Once more, this is not surprising, given that for more face-on systems the importance of higher modes increases, and they are both (i) more affected by the precession of the spins and

(ii) less well modeled in the aligned-spin limit. In this case, the global unfaithfulness is  $0.006^{+0.010}_{-0.003}$ , with the same notation as before. Overall, we find the performance of the model in the quasicircular precessing limit to be comparable to that of other state of the art models, by indirectly comparing to the results of Refs. [84,127].

## B. RIT:eBBH:1632

The performance of the model in the eccentric, precessing regime is tested via a time-domain comparison against the RIT simulation RIT:eBBH:1632, already discussed in Sec. III when considering the behavior of radiation-frame waveforms. Directly comparing waveforms in the inertial frame is not straightforward, as precessing waveforms are characterized by one additional degree of freedom with respect to the aligned-spin case: an initial angle  $\xi$  that determines the orientation of the in-plane spins. Therefore, comparing waveforms in the inertial frame would require devising a method to align them while varying three different parameters at the same time: initial eccentricity, initial anomaly and  $\xi$  (assuming a fixed initial orbit-averaged frequency). This can in principle be performed by, e.g., minimizing mismatches over a certain frequency range via either multi-dimensional numerical minimization or a simpler grid search [50]. Given the complex functional dependence of the waveform on the parameters, these methods are not expected to be particularly efficient, and typically require a large number of waveform evaluations to be performed to succeed. Therefore, rather than employing such a procedure, we

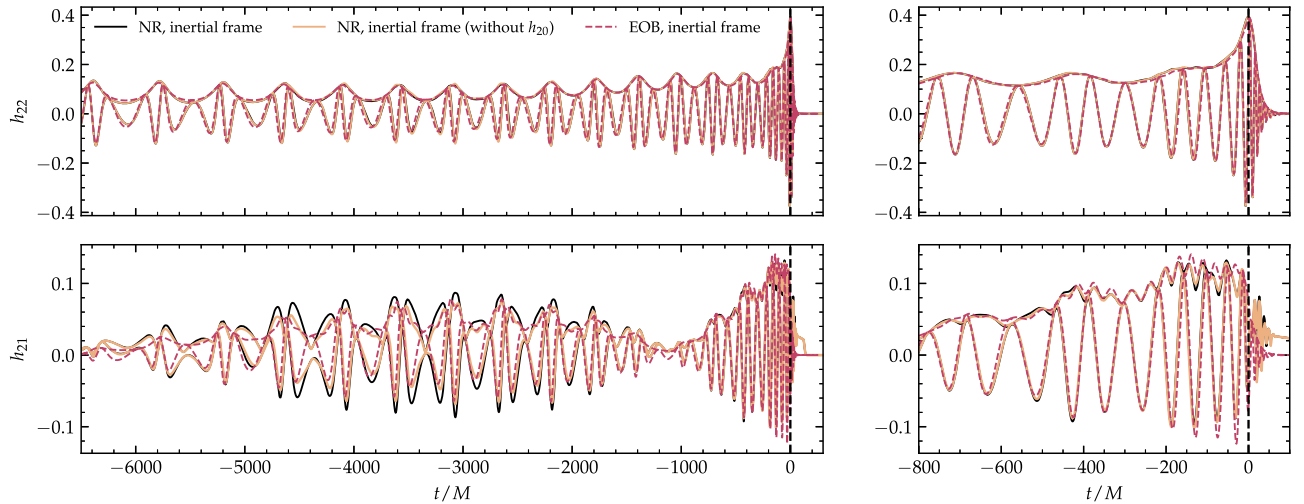


FIG. 12. Comparison between RIT NR waveform multipoles  $h_{\ell m} = (2, 2)$  and  $(2, 1)$  (black and orange lines) and the EOB model (red line) presented in this work. While the  $(2, 2)$  EOB and NR modes do not display large precession-induced modulations, the  $(2, 1)$  mode is clearly affected by the precession of the spins. For this mode, it is possible to observe large EOB/NR differences during the early inspiral ( $t \sim -5500$  to  $t \sim -3000$ ). It is not clear whether these differences are due to real inaccuracies of the EOB model, or rather can be reconduced to unphysical features of the simulation itself. Overall, our EOB model is able to capture the main features of the NR data in terms of both amplitude and phase evolution up to merger and beyond.

choose to focus on the  $(2, 2)$  mode and first find the eccentricity and anomaly  $e_0$  and  $\zeta_0$  that align the EOB waveform with the NR one in the coprecessing frame. Then—keeping these fixed—we vary  $\xi$  to obtain the  $\Delta t_{22}$ ,  $\Delta\phi_{22}$  values that provide the best alignment in the inertial frame. The initial conditions and shifts so obtained are used to also align the  $(2, 1)$  mode, recalling that  $\Delta\phi_{\ell m} = m/2\Delta\phi_{22}$ .

The results of this procedure are displayed in Fig. 12. The model correctly reproduces the amplitude peaks of the  $(2, 2)$  mode, as well as the less pronounced modulations due to the precession of the orbital plane. The  $(2, 1)$  mode in the inertial frame is computed entirely from the  $(2, |2|)$  coprecessing mode, and therefore it is more informative—in principle—regarding the performance of the model. We find that the EOB prediction is qualitatively consistent with the NR data, especially close to merger where the model approximates the amplitude modulations with remarkable accuracy ( $t \sim -400$  to  $-200$ ), and overall captures the envelope of the waveform amplitude. Gauging the quantitative performance of the model across the inspiral is more challenging, as unusual features appear in the NR waveform. Indeed, between the times of  $t \sim -5500$  and  $t \sim -3000$  the  $(2, 1)$  NR mode displays zeroes in the amplitude, which are not present in the

EOB prediction, as well as an overall “drift” (see Fig. 13). This effect was initially thought to be related to the presence of a nonzero  $(2, 0)$  coprecessing mode. However, after computing the NR radiation-frame modes, removing the  $(2, 0)$  and rotating back to the inertial frame, the presence of such zeroes does not appear to be significantly affected. The physical reality of this feature is therefore uncertain, and given that the merger-ringdown portion of the waveform appears significantly affected by errors in the simulation itself, the differences observed in the inspiral may be due to limitations in the NR data rather than in the EOB model.

## VI. CONCLUSIONS

In this work we discussed the phenomenology of eccentric, precessing BBHs in both the PN and NR regimes. After a brief review of the PN equations of motion for these kind of systems, we studied the morphology of the Euler angles  $\alpha$ ,  $\beta$ ,  $\gamma$  that connect the coprecessing,  $\mathcal{L}$ -aligned frame with the inertial frame for various kind of noncircular binaries (bound systems, eccentric and quasicircular, scatterings, captures), highlighting common features and differences. In view of the development of our noncircular, precessing model, we have assessed the importance of the explicitly noncircular contributions to the spin dynamics of the system, finding that they are largely negligible, even up to high values of  $e \sim 0.9$ . This result is in line with previous studies [77,78], and suggests that our model can be expected to be accurate up to such eccentricities. We have also briefly discussed the impact of precession on the scattering angle of low-energy BBH systems, finding again that spin precession does not significantly affect aspects of the orbital dynamics. Indeed, it contributes  $\lesssim 1\%$  to the azimuthal scattering angle, which displays a much stronger dependence on the mass ratio and the out-of-plane spin components, while generating usually only a modest deviation from the original orbital plane.

We then performed a preliminary study of eccentric, precessing numerical relativity simulations. We highlighted that the radiation-frame waveforms obtained by finding the direction of the tensor  $\langle \mathcal{L}_a \mathcal{L}_b \rangle$  are well approximated by aligned spins waveforms, and that the hierarchy of the modes in the coprecessing frame is consistent with that of aligned-spin systems. This is in line with the expectations from the quasicircular limit, and indicates that the twisting procedure routinely employed for these scenarios can be straightforwardly extended to the eccentric case. We also showed that, consistently with the PN results, the details of the orbit do not significantly affect the radiation-frame evolution, as one would expect from the separation of timescales between orbit, precession and backreaction.

Finally, we presented a model that is able to quantitatively describe the  $(2, 2)$  mode of the waveforms emitted by noncircularized systems. We discussed the different avenues that can be easily followed to extend any time domain eccentric waveform model to the precessing case, and

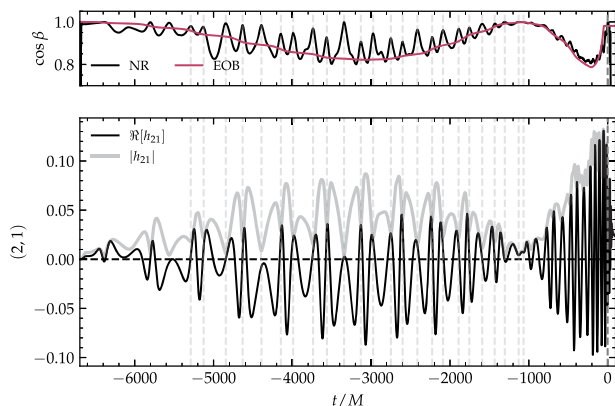


FIG. 13. Top: evolution of the Euler angle  $\beta$  extracted from the RIT:eBBH:1632 simulation (black) and the EOB prediction (red). Bottom: real part (black) and amplitude (gray) of the inertial-frame  $(2,1)$  mode of the same NR simulation. We highlight with dashed vertical lines the minima of the amplitude of the  $(2,1)$  mode between  $-5500M$  and  $-1000M$ , which are not present in the EOB prediction: they correspond to the times when the  $\beta$  angle extracted from the NR simulation is closest to 0. These spikes in  $\beta$  do not, however, clearly correspond to periastron or apastron passages, or other reference points in the orbit. A noticeable “drift” can be observed from the real part of the NR waveform, which does not oscillate around  $y = 0$ . Recalling that the NR Euler angles are extracted by identifying the radiation frame from the waveform modes, it apparent that this drift is closely related to the behavior of the NR  $\beta$ . What remains unclear is whether it is due to a real physical effect, which induces oscillations in  $\beta$  reflected in the inertial-frame waveform, or rather to inaccuracies in the NR data itself, which are then reflected in the calculation of Euler angles.

chose to adopt the simplest one, which is based on the orbit-averaged expressions for the spin dynamics of Ref. [49]. We then presented the first results of this model, showing that it is faithful to NR simulations in the quasicircular limit, and performing one EOB/NR comparison for the largest eccentricity simulation (with precession) in the RIT database with more than 10 orbital cycles. While the model appears to be accurate up to merger and beyond in the (2, 2) mode, the behavior of the (2, 1) mode is only qualitatively captured during the inspiral. It is unclear whether this is due to limitations of the EOB model or inaccuracies of the NR data itself.

As the community slowly undertakes the endeavor of producing new highly accurate, eccentric, precessing NR simulations, the EOB model presented in this work should be considered as a predictive tool, *a posteriori* confirmed (or falsified) by NR. Along these lines, in future works we will perform a more in-depth NR validation of the model within this challenging regime. This will allow us to clearly identify its limitations and define its current range of applicability, indicating avenues for future improvements. At the same time, we also aim to incorporate the description of the (2, 0) mode, known to be significant for highly eccentric systems, and—more ambitiously—to build a full IMR model accounting for noncircularity and precession also beyond merger. In doing so, we anticipate refining our understanding of eccentric, nonplanar coalescing CBCs, ultimately enriching our comprehension of these complex systems.

## ACKNOWLEDGMENTS

The authors warmly thank the anonymous referee for their insightful comments. In particular, point (iii) of the list in Sec. IV C stems from the referee’s suggestion, which the authors merely expanded upon and for which they do not claim any intellectual credit. The authors also wish to thank G. Pratten, G. Carullo, A. Nagar, S. Bernuzzi, D. Radice and B. Sathyaprakash for useful discussions and feedback. R. G. and D. C. additionally thank A. “Nali” Scarrone, D. Rettore and A. Mango for inspiring them throughout the development of this work. Finally, the authors wish to thank the MAYA, RIT and SXS collaborations for sharing their simulations and maintaining their public databases. R. G. acknowledges support by the Deutsche Forschungsgemeinschaft (DFG) under Grant No. 406116891 within the Research Training Group RTG 2522/1 and from NSF Grant No. PHY-2020275 [Network for Neutrinos, Nuclear Astrophysics, and Symmetries (N3AS)]. D. C. acknowledges support from the Italian Ministry of University and Research (MUR) via the PRIN 2022ZHYFA2, *Gravitational waveform models for coalescing compact binaries with*

*eccentricity* (GREAT). S. N. acknowledges support from DAAD for funding. TEOBResumS is publicly available at [128]. The version employed in this work is tagged via the arXiv submission number of the paper itself.

## APPENDIX: PN INITIAL CONDITIONS

Section II of this work relies on the integration of the PN equations of motion (Eqs. (1)) for different kinds of orbital dynamics: quasicircular, eccentric and hyperbolic (or capture). Orbits corresponding to these three main families are realized by choosing appropriate initial conditions, i.e., values of the initial radial separation and velocity. In this Appendix we provide expressions for computing the initial conditions for eccentric and hyperbolic orbits in terms of more convenient sets of parameters: eccentricity and semilatus rectum for the former, and energy and angular momentum for the latter. As already mentioned in the main text, we neglect spin-orbit terms in the expressions for the energy and angular momentum that we use to set up the initial conditions (they are included in the equations of motion); their impact is expected to be small, and this approximation does not invalidate the conclusions of our study of the PN dynamics.

In the expressions in this Appendix we include explicit powers of  $1/c$  to keep track of PN order.

### 1. Eccentric orbits

We define the eccentricity  $e$  and semilatus rectum  $p$  by their relation to the periastron and apastron radii  $r_{p,a}$ , as in Newtonian gravity:

$$r_p = \frac{p}{1+e}, \quad r_a = \frac{p}{1-e}. \quad (\text{A1})$$

To calculate the velocities  $v_{p,a}$  at the extremes of the orbit we use the 3PN expressions for the energy and angular momentum as functions of  $r$ ,  $v$  and  $\dot{r}$  given in Eq. (23) of [129]: we require that both  $\hat{E} = E/\mu$  and  $\hat{L} = L/\mu$  have the same value when evaluated at periastron and apastron, and solve the resulting system of equations for the PN-expanded  $v_{p,a}(e, p)$

$$\hat{E}(r_p, v_p, \dot{r} = 0) = \hat{E}(r_a, v_a, \dot{r} = 0) \quad (\text{A2})$$

$$\hat{L}(r_p, v_p, \dot{r} = 0) = \hat{L}(r_a, v_a, \dot{r} = 0). \quad (\text{A3})$$

We show here the result for the periastron velocity  $v_p(e, p)$ , where we start our eccentric orbits

$$\begin{aligned}
v_p = \frac{1+e}{\sqrt{p}} \left\{ 1 + \frac{1}{2pc^2} [e^2 + 8e(\nu-1) - \nu - 3] + \frac{1}{8p^2c^4} [e^4(-24\nu^2 + 8\nu + 3) + 4e^3(6\nu^2 - 7\nu - 4) \right. \\
+ e^2(48\nu^2 - 135\nu + 58) + 8e(9\nu^2 - 6\nu + 8) - 41\nu^2 + 111\nu + 15] \\
+ \frac{1}{p^3c^6} \left[ e^6 \left( \frac{61\nu^3}{8} - \frac{91\nu^2}{8} + 3\nu + \frac{5}{16} \right) + e^5 \left( -\frac{69\nu^3}{4} + \frac{125\nu^2}{4} - \frac{113\nu}{8} - \frac{3}{2} \right) \right. \\
+ e^4 \left( -\frac{137\nu^3}{8} + \frac{203\nu^2}{8} + \frac{(4305\pi^2 - 123848)\nu}{13440} + \frac{47}{16} \right) + e^3 \left( 53\nu^3 - \frac{531\nu^2}{4} + \frac{(391108 - 4305\pi^2)\nu}{3360} - 8 \right) \\
+ e^2 \left( \frac{59\nu^3}{8} - \frac{77\nu^2}{4} + \frac{(51608 - 1435\pi^2)\nu}{2240} - \frac{313}{16} \right) + e \left( -\frac{13\nu^3}{4} + \frac{279\nu^2}{4} + \frac{(-29696 - 12915\pi^2)\nu}{3360} - \frac{29}{2} \right) \\
\left. - \frac{79\nu^3}{16} + \frac{141\nu^2}{8} + \frac{(4305\pi^2 - 855976)\nu}{13440} - \frac{35}{16} \right\} \quad (\text{A4})
\end{aligned}$$

## 2. Hyperbolic orbits

For hyperbolic orbits, we choose the initial values of the energy  $\hat{E}_0$  and orbital angular momentum  $\hat{L}_0$ , as well as the starting orbital separation  $r$ . We then invert the PN-expanded expressions of the energy and angular momentum (Eq. 23 of [129]) to find the radial and azimuthal components of the velocity vector

$$\begin{aligned}
v_r^2 = 2\hat{E}_0 - \frac{\hat{L}_0^2}{r^2} + \frac{2}{r} + \frac{1}{c^2} \left[ \hat{E}_0^2(9\nu - 3) + \frac{\hat{E}_0\hat{L}_0^2}{r^2}(2 - 6\nu) + \frac{1}{r^2}(5\nu - 10) + \frac{\hat{E}_0}{r}(14\nu - 12) + \frac{\hat{L}_0^2}{r^3}(8 - 7\nu) \right] \\
+ \frac{1}{c^4} \left[ \hat{E}_0^3(16\nu^2 - 19\nu + 4) + \frac{\hat{E}_0^2\hat{L}_0^2}{r^2}(-15\nu^2 + 15\nu - 3) + \frac{\hat{E}_0}{r^2}(36\nu^2 - 127\nu + 36) + \frac{\hat{E}_0^2}{r}(42\nu^2 - 96\nu + 18) \right. \\
+ \left. \frac{\hat{E}_0\hat{L}_0^2}{r^3}(-55\nu^2 + 73\nu - 16) + \frac{1}{r^3} \left( 10\nu^2 - \frac{81\nu}{2} + 26 \right) + \frac{\hat{L}_0^4}{r^5} \left( \frac{15\nu}{4} - \frac{\nu^2}{4} \right) + \frac{\hat{L}_0^2}{r^4} \left( -38\nu^2 + \frac{267\nu}{4} - 33 \right) \right] \\
+ \frac{1}{c^6} \left[ \hat{E}_0^4 \left( 14\nu^3 - \frac{211\nu^2}{4} + 32\nu - 5 \right) + \frac{\hat{E}_0^3}{r}(70\nu^3 - 342\nu^2 + 186\nu - 24) + \frac{\hat{E}_0\hat{L}_0^2}{r^3} \left( -192\nu^3 + \frac{651\nu^2}{2} - 168\nu + 24 \right) \right. \\
+ \frac{\hat{E}_0}{r^3} \left( 74\nu^3 - \frac{911\nu^2}{2} + \frac{41\pi^2\nu}{8} + \frac{165353\nu}{210} - 76 \right) + \frac{\hat{E}_0^3\hat{L}_0^2}{r^2}(-20\nu^3 + 50\nu^2 - 27\nu + 4) + \frac{\hat{E}_0^2}{r^2} \left( 114\nu^3 - 659\nu^2 \right. \\
+ \left. \frac{1738\nu}{3} - 54 \right) + \frac{\hat{E}_0\hat{L}_0^2}{r^4} \left( -366\nu^3 + \frac{1439\nu^2}{2} - \frac{2463\nu}{4} + 66 \right) + \frac{1}{r^4} \left( 16\nu^3 - \frac{403\nu^2}{4} + \frac{41\pi^2\nu}{8} + \frac{60341\nu}{210} - 50 \right) \\
+ \frac{\hat{E}_0\hat{L}_0^4}{r^5} \left( -\frac{27\nu^3}{4} + \frac{241\nu^2}{4} - \frac{71\nu}{4} \right) + \frac{\hat{L}_0^2}{r^5} \left( -186\nu^3 + 392\nu^2 - \frac{41\pi^2\nu}{32} - \frac{36929\nu}{70} + 96 \right) \\
\left. + \frac{\hat{L}_0^6}{r^7} \left( \frac{13\nu^3}{8} - \frac{73\nu^2}{8} + \frac{23\nu}{8} \right) + \frac{\hat{L}_0^4}{r^6} \left( -6\nu^3 + \frac{667\nu^2}{8} - \frac{11\nu}{8} \right) \right] \quad (\text{A5})
\end{aligned}$$

$$\begin{aligned}
v_\phi = \frac{\hat{L}_0}{r} \left\{ 1 + \frac{1}{c^2} \left[ \hat{E}_0(-1 + 3\nu) + \frac{-4 + 4\nu}{r} \right] + \frac{1}{c^4} \left[ \frac{\hat{L}_0^2}{r^3} \left( -\frac{3}{2}\nu - \nu^2 \right) + \hat{E}_0^2 \left( 1 - \frac{9\nu}{2} + 3\nu^2 \right) + \frac{1}{r^2} \left( 9 - \frac{67}{4}\nu + 17\nu^2 \right) \right. \right. \\
+ \left. \frac{\hat{E}_0}{r} (4 - 24\nu + 20\nu^2) \right] + \frac{1}{c^6} \left[ \frac{\hat{L}_0^2}{r^4} \left( \frac{11\nu}{12} - \frac{75\nu^2}{4} - 15\nu^3 \right) + \frac{\hat{L}_0^4}{r^5} \left( -\frac{9\nu}{8} + 3\nu^2 + \frac{3\nu^3}{4} \right) + \hat{E}_0^3 \left( -1 + 6\nu - \frac{17\nu^2}{2} + \nu^3 \right) \right. \\
+ \frac{\hat{E}_0^2}{r} (-4 + 34\nu - 76\nu^2 + 42\nu^3) + \frac{1}{r^3} \left( -16 + \frac{74677\nu}{840} - \frac{41\pi^2\nu}{32} - \frac{157\nu^2}{2} + 74\nu^3 \right) \\
\left. + \frac{\hat{E}_0\hat{L}_0^2}{r^3} (4\nu - 12\nu^2 - 6\nu^3) + \frac{\hat{E}_0}{r^2} \left( -9 + \frac{1615\nu}{12} - \frac{699\nu^2}{4} + 117\nu^3 \right) \right] \left. \right\} \quad (\text{A6})
\end{aligned}$$

- [1] B. P. Abbott *et al.* (LIGO Scientific, VIRGO, Las Cumbres Observatory, DLT40, Virgo, 1M2H, and MASTER Collaborations), A gravitational-wave standard siren measurement of the Hubble constant, *Nature (London)* **551**, 85 (2017).
- [2] Benjamin P. Abbott *et al.* (Virgo and LIGO Scientific Collaborations), GW170817: Observation of gravitational waves from a binary neutron star inspiral, *Phys. Rev. Lett.* **119**, 161101 (2017).
- [3] B. P. Abbott *et al.* (LIGO Scientific and Virgo Collaborations), GW170817: Measurements of neutron star radii and equation of state, *Phys. Rev. Lett.* **121**, 161101 (2018).
- [4] Eemeli Annala, Tyler Gorda, Alekski Kurkela, and Alekski Vuorinen, Gravitational-wave constraints on the neutron-star-matter equation of state, *Phys. Rev. Lett.* **120**, 172703 (2018).
- [5] David Radice, Albino Perego, Kenta Hotokezaka, Steven A. Fromm, Sebastiano Bernuzzi, and Luke F. Roberts, Binary neutron star mergers: Mass ejection, electromagnetic counterparts and nucleosynthesis, *Astrophys. J.* **869**, 130 (2018).
- [6] Soumi De, Daniel Finstad, James M. Lattimer, Duncan A. Brown, Edo Berger, and Christopher M. Biwer, Tidal deformabilities and radii of neutron stars from the observation of GW170817, *Phys. Rev. Lett.* **121**, 091102 (2018); **121**, 259902(E) (2018).
- [7] F. J. Fattoyev, J. Piekarewicz, and C. J. Horowitz, Neutron skins and neutron stars in the multi-messenger era, *Phys. Rev. Lett.* **120**, 172702 (2018).
- [8] Elias R. Most, Lukas R. Weih, Luciano Rezzolla, and Jürgen Schaffner-Bielich, New constraints on radii and tidal deformabilities of neutron stars from GW170817, *Phys. Rev. Lett.* **120**, 261103 (2018).
- [9] Carolyn Raithel, Feryal Özel, and Dimitrios Psaltis, Tidal deformability from GW170817 as a direct probe of the neutron star radius, *Astrophys. J. Lett.* **857**, L23 (2018).
- [10] I. Tews, J. Margueron, and S. Reddy, Critical examination of constraints on the equation of state of dense matter obtained from GW170817, *Phys. Rev. C* **98**, 045804 (2018).
- [11] J. Meidam, M. Agathos, C. Van Den Broeck, J. Veitch, and B. S. Sathyaprakash, Testing the no-hair theorem with black hole ringdowns using TIGER, *Phys. Rev. D* **90**, 064009 (2014).
- [12] B. P. Abbott *et al.* (LIGO Scientific and Virgo Collaborations), Tests of general relativity with GW150914, *Phys. Rev. Lett.* **116**, 221101 (2016); **121**, 129902(E) (2018).
- [13] B. P. Abbott *et al.* (LIGO Scientific and Virgo Collaborations), Tests of general relativity with GW170817, *Phys. Rev. Lett.* **123**, 011102 (2019).
- [14] R. Abbott *et al.* (LIGO Scientific and Virgo Collaborations), GWTC-2: Compact binary coalescences observed by LIGO and Virgo during the first half of the third observing run, *Phys. Rev. X* **11**, 021053 (2021).
- [15] R. Abbott *et al.* (LIGO Scientific and Virgo Collaborations), GW190412: Observation of a binary-black-hole coalescence with asymmetric masses, *Phys. Rev. D* **102**, 043015 (2020).
- [16] R. Abbott *et al.* (KAGRA, VIRGO, and LIGO Scientific Collaborations), GWTC-3: Compact binary coalescences observed by LIGO and Virgo during the second part of the third observing run, *Phys. Rev. X* **13**, 041039 (2023).
- [17] Vijay Varma, Sylvia Biscoveanu, Tousif Islam, Feroz H. Shaik, Carl-Johan Haster, Maximiliano Isi, Will M. Farr, Scott E. Field, and Salvatore Vitale, Evidence of large recoil velocity from a black hole merger signal, *Phys. Rev. Lett.* **128**, 191102 (2022).
- [18] R. Abbott *et al.* (LIGO Scientific and Virgo Collaborations), GW190521: A binary black hole merger with a total mass of  $150M_{\odot}$ , *Phys. Rev. Lett.* **125**, 101102 (2020).
- [19] R. Abbott *et al.* (LIGO Scientific and Virgo Collaborations), Properties and astrophysical implications of the 150 Msun binary black hole merger GW190521, *Astrophys. J. Lett.* **900**, L13 (2020).
- [20] B. P. Abbott *et al.* (LIGO Scientific, Virgo, Fermi GBM, INTEGRAL, IceCube, AstroSat Cadmium Zinc Telluride Imager Team, IPN, Insight-Hxmt, ANTARES, Swift, AGILE Team, 1M2H Team, Dark Energy Camera GW-EM, DES, DLT40, GRAWITA, Fermi-LAT, ATCA, ASKAP, Las Cumbres Observatory Group, OzGrav, DWF (Deeper Wider Faster Program), AST3, CAASTRO, VIRGO, MASTER, J-GEM, GROWTH, JAGWAR, CaltechNRAO, TTU-NRAO, NuSTAR, Pan-STARRS, MAXI Team, TZAC Consortium, KU, Nordic Optical Telescope, ePESSTO, GROND, Texas Tech University, SALT Group, TOROS, BOOTES, MWA, CALET, IKI-GW Follow-up, H.E.S.S., LOFAR, LWA, HAWC, Pierre Auger, ALMA, Euro VLBI Team, Pi of Sky, Chandra Team at McGill University, DFN, ATLAS Telescopes, High Time Resolution Universe Survey, RIMAS, RATIR, and SKA South Africa/MeerKAT Collaborations), Multimessenger observations of a binary neutron star merger, *Astrophys. J. Lett.* **848**, L12 (2017).
- [21] B. P. Abbott *et al.* (LIGO Scientific and Virgo Collaborations), GW190425: Observation of a compact binary coalescence with total mass  $\sim 3.4M_{\odot}$ , *Astrophys. J. Lett.* **892**, L3 (2020).
- [22] R. Abbott *et al.* (LIGO Scientific, KAGRA, and VIRGO Collaborations), Observation of gravitational waves from two neutron star-black hole coalescences, *Astrophys. J. Lett.* **915**, L5 (2021).
- [23] V. Gayathri, J. Healy, J. Lange, B. O'Brien, M. Szczepanczyk, Imre Bartos, M. Campanelli, S. Klimentenko, C. O. Lousto, and R. O'Shaughnessy, Eccentricity estimate for black hole mergers with numerical relativity simulations, *Nat. Astron.* **6**, 344 (2022).
- [24] Isobel M. Romero-Shaw, Paul D. Lasky, Eric Thrane, and Juan Calderon Bustillo, GW190521: Orbital eccentricity and signatures of dynamical formation in a binary black hole merger signal, *Astrophys. J. Lett.* **903**, L5 (2020).
- [25] Juan Calderón Bustillo, Nicolas Sanchis-Gual, Alejandro Torres-Forné, and José A. Font, Confusing head-on collisions with precessing intermediate-mass binary black hole mergers, *Phys. Rev. Lett.* **126**, 201101 (2021).
- [26] Masaru Shibata, Kenta Kiuchi, Sho Fujibayashi, and Yuichiro Sekiguchi, Alternative possibility of GW190521: Gravitational waves from high-mass black hole-disk systems, *Phys. Rev. D* **103**, 063037 (2021).

- [27] Alexander H. Nitz and Collin D. Capano, GW190521 may be an intermediate mass ratio inspiral, *Astrophys. J. Lett.* **907**, L9 (2021).
- [28] Rossella Gamba, Matteo Breschi, Gregorio Carullo, Simone Albanesi, Piero Rettegno, Sebastiano Bernuzzi, and Alessandro Nagar, GW190521 as a dynamical capture of two nonspinning black holes, *Nat. Astron.* **7**, 11 (2023).10.1038/s41550-022-01813-w
- [29] Isobel M. Romero-Shaw, Davide Gerosa, and Nicholas Loutrel, Eccentricity or spin precession? Distinguishing subdominant effects in gravitational-wave data, *Mon. Not. R. Astron. Soc.* **519**, 5352 (2023).
- [30] Koustav Chandra, Archana Pai, Samson H. W. Leong, and Juan Calderón Bustillo, Impact of Bayesian priors on the inferred masses of quasicircular intermediate-mass black hole binaries, *Phys. Rev. D* **109**, 104031 (2024).
- [31] Theocharis A. Apostolatos, Curt Cutler, Gerald J. Sussman, and Kip S. Thorne, Spin induced orbital precession and its modulation of the gravitational wave forms from merging binaries, *Phys. Rev. D* **49**, 6274 (1994).
- [32] Alessandra Buonanno, Yan-bei Chen, and Michele Vallisneri, Detecting gravitational waves from precessing binaries of spinning compact objects: Adiabatic limit, *Phys. Rev. D* **67**, 104025 (2003); **74**, 029904(E) (2006).
- [33] Patricia Schmidt, Mark Hannam, Sascha Husa, and P. Ajith, Tracking the precession of compact binaries from their gravitational-wave signal, *Phys. Rev. D* **84**, 024046 (2011).
- [34] Patricia Schmidt, Mark Hannam, and Sascha Husa, Towards models of gravitational waveforms from generic binaries: A simple approximate mapping between precessing and nonprecessing inspiral signals, *Phys. Rev. D* **86**, 104063 (2012).
- [35] Michael Boyle, Robert Owen, and Harald P. Pfeiffer, A geometric approach to the precession of compact binaries, *Phys. Rev. D* **84**, 124011 (2011).
- [36] R. O’Shaughnessy, B. Vaishnav, J. Healy, Z. Meeks, and D. Shoemaker, Efficient asymptotic frame selection for binary black hole spacetimes using asymptotic radiation, *Phys. Rev. D* **84**, 124002 (2011).
- [37] Yi Pan, Alessandra Buonanno, Andrea Taracchini, Lawrence E. Kidder, Abdul H. Mroué, Harald P. Pfeiffer, Mark A. Scheel, and Béla Szilágyi, Inspiral-merger-ringdown waveforms of spinning, precessing black-hole binaries in the effective-one-body formalism, *Phys. Rev. D* **89**, 084006 (2014).
- [38] Jonathan E. Thompson, Eleanor Hamilton, Lionel London, Shrobona Ghosh, Panagiota Kolitsidou, Charlie Hoy, and Mark Hannam, Phenomenological gravitational-wave model for precessing black-hole binaries with higher multipoles and asymmetries, *Phys. Rev. D* **109**, 063012 (2024).
- [39] Shrobona Ghosh, Panagiota Kolitsidou, and Mark Hannam, First frequency-domain phenomenological model of the multipole asymmetry in gravitational-wave signals from binary-black-hole coalescence, *Phys. Rev. D* **109**, 024061 (2024).
- [40] Eleanor Hamilton, Lionel London, and Mark Hannam, Ringdown frequencies in black holes formed from precessing black-hole binaries, *Phys. Rev. D* **107**, 104035 (2023).
- [41] Lionel London, Sebastian Khan, Edward Fauchon-Jones, Xisco Jiménez Forteza, Mark Hannam, Sascha Husa, Chinmay Kalaghatgi, Frank Ohme, and Francesco Pannarale, First higher-multipole model of gravitational waves from spinning and coalescing black-hole binaries, *Phys. Rev. Lett.* **120**, 161102 (2018).
- [42] Cecilio García-Quirós, Marta Colleoni, Sascha Husa, Héctor Estellés, Geraint Pratten, Antoni Ramos-Buades, Maite Mateu-Lucena, and Rafel Jaume, Multimode frequency-domain model for the gravitational wave signal from nonprecessing black-hole binaries, *Phys. Rev. D* **102**, 064002 (2020).
- [43] Sebastian Khan, Frank Ohme, Katerina Chatziioannou, and Mark Hannam, Including higher order multipoles in gravitational-wave models for precessing binary black holes, *Phys. Rev. D* **101**, 024056 (2020).
- [44] Mark Hannam, Patricia Schmidt, Alejandro Bohé, Leïla Haegel, Sascha Husa, Frank Ohme, Geraint Pratten, and Michael Pürrer, Simple model of complete precessing black-hole-binary gravitational waveforms, *Phys. Rev. Lett.* **113**, 151101 (2014).
- [45] Patricia Schmidt, Frank Ohme, and Mark Hannam, Towards models of gravitational waveforms from generic binaries II: Modelling precession effects with a single effective precession parameter, *Phys. Rev. D* **91**, 024043 (2015).
- [46] Sebastian Khan, Katerina Chatziioannou, Mark Hannam, and Frank Ohme, Phenomenological model for the gravitational-wave signal from precessing binary black holes with two-spin effects, *Phys. Rev. D* **100**, 024059 (2019).
- [47] Geraint Pratten *et al.*, Computationally efficient models for the dominant and subdominant harmonic modes of precessing binary black holes, *Phys. Rev. D* **103**, 104056 (2021).
- [48] Serguei Ossokine *et al.*, Multipolar effective-one-body waveforms for precessing binary black holes: Construction and validation, *Phys. Rev. D* **102**, 044055 (2020).
- [49] Sarp Akcay, Rossella Gamba, and Sebastiano Bernuzzi, A hybrid post-Newtonian–effective-one-body scheme for spin-precessing compact-binary waveforms, *Phys. Rev. D* **103**, 024014 (2021).
- [50] Antoni Ramos-Buades, Alessandra Buonanno, Héctor Estellés, Mohammed Khalil, Deyan P. Mihaylov, Serguei Ossokine, Lorenzo Pompili, and Mahlet Shiferaw, Next generation of accurate and efficient multipolar precessing-spin effective-one-body waveforms for binary black holes, *Phys. Rev. D* **108**, 124037 (2023).
- [51] A. Buonanno and T. Damour, Effective one-body approach to general relativistic two-body dynamics, *Phys. Rev. D* **59**, 084006 (1999).
- [52] Alessandra Buonanno and Thibault Damour, Transition from inspiral to plunge in binary black hole coalescences, *Phys. Rev. D* **62**, 064015 (2000).
- [53] Thibault Damour, Piotr Jaranowski, and Gerhard Schafer, On the determination of the last stable orbit for circular general relativistic binaries at the third postNewtonian approximation, *Phys. Rev. D* **62**, 084011 (2000).

- [54] Thibault Damour, Coalescence of two spinning black holes: An effective one-body approach, *Phys. Rev. D* **64**, 124013 (2001).
- [55] Thibault Damour, Piotr Jaranowski, and Gerhard Schäfer, Effective one body approach to the dynamics of two spinning black holes with next-to-leading order spin-orbit coupling, *Phys. Rev. D* **78**, 024009 (2008).
- [56] Alessandro Nagar, Effective one body Hamiltonian of two spinning black-holes with next-to-next-to-leading order spin-orbit coupling, *Phys. Rev. D* **84**, 084028 (2011).
- [57] Thibault Damour, Piotr Jaranowski, and Gerhard Schäfer, Fourth post-Newtonian effective one-body dynamics, *Phys. Rev. D* **91**, 084024 (2015).
- [58] Ian Hinder, Lawrence E. Kidder, and Harald P. Pfeiffer, An eccentric binary black hole inspiral-merger-ringdown gravitational waveform model from numerical relativity and post-Newtonian theory, *Phys. Rev. D* **98**, 044015 (2018).
- [59] Tousif Islam, Study of eccentric binary black hole mergers using numerical relativity and an inspiral-merger-ringdown model, [arXiv:2403.03487](https://arxiv.org/abs/2403.03487).
- [60] Tousif Islam, Vijay Varma, Jackie Lodman, Scott E. Field, Gaurav Khanna, Mark A. Scheel, Harald P. Pfeiffer, Davide Gerosa, and Lawrence E. Kidder, Eccentric binary black hole surrogate models for the gravitational waveform and remnant properties: Comparable mass, nonspinning case, *Phys. Rev. D* **103**, 064022 (2021).
- [61] Thibault Damour, Federico Guercilena, Ian Hinder, Seth Hopper, Alessandro Nagar, and Luciano Rezzolla, Strong-field scattering of two black holes: Numerics versus analytics, *Phys. Rev. D* **89**, 081503 (2014).
- [62] Tanja Hinderer and Stanislav Babak, Foundations of an effective-one-body model for coalescing binaries on eccentric orbits, *Phys. Rev. D* **96**, 104048 (2017).
- [63] Zhoujian Cao and Wen-Biao Han, Waveform model for an eccentric binary black hole based on the effective-one-body-numerical-relativity formalism, *Phys. Rev. D* **96**, 044028 (2017).
- [64] Xiaolin Liu, Zhoujian Cao, and Zong-Hong Zhu, A higher-multipole gravitational waveform model for an eccentric binary black holes based on the effective-one-body-numerical-relativity formalism, *Classical Quantum Gravity* **39**, 035009 (2022).
- [65] Xiaolin Liu, Zhoujian Cao, and Lijing Shao, Upgraded waveform model of eccentric binary black hole based on effective-one-body-numerical-relativity for spin-aligned binary black holes, *Int. J. Mod. Phys. D* **32**, 2350015 (2023).
- [66] Danilo Chiamello and Alessandro Nagar, Faithful analytical effective-one-body waveform model for spin-aligned, moderately eccentric, coalescing black hole binaries, *Phys. Rev. D* **101**, 101501 (2020).
- [67] Alessandro Nagar, Alice Bonino, and Piero Rettegno, Effective one-body multipolar waveform model for spin-aligned, quasicircular, eccentric, hyperbolic black hole binaries, *Phys. Rev. D* **103**, 104021 (2021).
- [68] Alessandro Nagar and Piero Rettegno, Next generation: Impact of high-order analytical information on effective one body waveform models for noncircularized, spin-aligned black hole binaries, *Phys. Rev. D* **104**, 104004 (2021).
- [69] Alessandro Nagar, Piero Rettegno, Rossella Gamba, Simone Albanesi, Angelica Albertini, and Sebastiano Bernuzzi, Analytic systematics in next generation of effective-one-body gravitational waveform models for future observations, *Phys. Rev. D* **108**, 124018 (2023).
- [70] Antoni Ramos-Buades, Alessandra Buonanno, Mohammed Khalil, and Serguei Ossokine, Effective-one-body multipolar waveforms for eccentric binary black holes with non-precessing spins, *Phys. Rev. D* **105**, 044035 (2022).
- [71] Mohammed Khalil, Alessandra Buonanno, Jan Steinhoff, and Justin Vines, Radiation-reaction force and multipolar waveforms for eccentric, spin-aligned binaries in the effective-one-body formalism, *Phys. Rev. D* **104**, 024046 (2021).
- [72] Andrea Placidi, Simone Albanesi, Alessandro Nagar, Marta Orselli, Sebastiano Bernuzzi, and Gianluca Grignani, Exploiting Newton-factorized, 2PN-accurate waveform multipoles in effective-one-body models for spin-aligned noncircularized binaries, *Phys. Rev. D* **105**, 104030 (2022).
- [73] Simone Albanesi, Alessandro Nagar, Sebastiano Bernuzzi, Andrea Placidi, and Marta Orselli, Assessment of effective-one-body radiation reactions for generic planar orbits, *Phys. Rev. D* **105**, 104031 (2022).
- [74] Antoine Klein, Yannick Boetzel, Achamveedu Gopakumar, Philippe Jetzer, and Lorenzo de Vittori, Fourier domain gravitational waveforms for precessing eccentric binaries, *Phys. Rev. D* **98**, 104043 (2018).
- [75] Khun Sang Phukon, Anuradha Gupta, Sukanta Bose, and Pankaj Jain, Effect of orbital eccentricity on the dynamics of precessing compact binaries, *Phys. Rev. D* **100**, 124008 (2019).
- [76] Antoine Klein, EFPE: Efficient fully precessing eccentric gravitational waveforms for binaries with long inspirals, [arXiv:2106.10291](https://arxiv.org/abs/2106.10291).
- [77] Brennan Ireland, Ofek Birnholtz, Hiroyuki Nakano, Eric West, and Manuela Campanelli, Eccentric binary black holes with spin via the direct integration of the post-Newtonian equations of motion, *Phys. Rev. D* **100**, 024015 (2019).
- [78] Giulia Fumagalli and Davide Gerosa, Spin-eccentricity interplay in merging binary black holes, *Phys. Rev. D* **108**, 124055 (2023).
- [79] J. Nijaid Arredondo, Antoine Klein, and Nicolás Yunes, Efficient gravitational-wave model for fully-precessing and moderately-eccentric, compact binary inspirals, [arXiv:2402.06804](https://arxiv.org/abs/2402.06804).
- [80] Xiaolin Liu, Zhoujian Cao, and Zong-Hong Zhu, Effective-one-body numerical-relativity waveform model for eccentric spin-precessing binary black hole coalescence, [arXiv:2310.04552](https://arxiv.org/abs/2310.04552).
- [81] Alejandro Bohé *et al.*, Improved effective-one-body model of spinning, nonprecessing binary black holes for the era of gravitational-wave astrophysics with advanced detectors, *Phys. Rev. D* **95**, 044028 (2017).
- [82] Roberto Cotesta, Alessandra Buonanno, Alejandro Bohé, Andrea Taracchini, Ian Hinder, and Serguei Ossokine, Enriching the symphony of gravitational waves from binary black holes by tuning higher harmonics, *Phys. Rev. D* **98**, 084028 (2018).

- [83] James Healy and Carlos O. Lousto, Fourth RIT binary black hole simulations catalog: Extension to eccentric orbits, *Phys. Rev. D* **105**, 124010 (2022).
- [84] Rossella Gamba, Sarp Akçay, Sebastiano Bernuzzi, and Jake Williams, Effective-one-body waveforms for precessing coalescing compact binaries with post-Newtonian twist, *Phys. Rev. D* **106**, 024020 (2022).
- [85] Alejandro Bohe, Sylvain Marsat, Guillaume Faye, and Luc Blanchet, Next-to-next-to-leading order spin-orbit effects in the near-zone metric and precession equations of compact binaries, *Classical Quantum Gravity* **30**, 075017 (2013).
- [86] Luc Blanchet, Gravitational radiation from post-Newtonian sources and inspiralling compact binaries, *Living Rev. Relativity* **17**, 2 (2014).
- [87] Nick Tacik *et al.*, Binary neutron stars with arbitrary spins in numerical relativity, *Phys. Rev. D* **92**, 124012 (2015); **94**, 049903(E) (2016).
- [88] Wolfgang Tichy, Alireza Rashti, Tim Dietrich, Reetika Dudi, and Bernd Brügmann, Constructing binary neutron star initial data with high spins, high compactness, and high mass-ratios, *Phys. Rev. D* **100**, 124046 (2019).
- [89] Etienne Racine, Analysis of spin precession in binary black hole systems including quadrupole-monopole interaction, *Phys. Rev. D* **78**, 044021 (2008).
- [90] Lucy M. Thomas, Patricia Schmidt, and Geraint Pratten, New effective precession spin for modeling multimodal gravitational waveforms in the strong-field regime, *Phys. Rev. D* **103**, 083022 (2021).
- [91] Seth Hopper, Alessandro Nagar, and Piero Retegno, Strong-field scattering of two spinning black holes: Numerics versus analytics, *Phys. Rev. D* **107**, 124034 (2023).
- [92] Thibault Damour and Piero Retegno, Strong-field scattering of two black holes: Numerical relativity meets post-Minkowskian gravity, *Phys. Rev. D* **107**, 064051 (2023).
- [93] Piero Retegno, Geraint Pratten, Lucy M. Thomas, Patricia Schmidt, and Thibault Damour, Strong-field scattering of two spinning black holes: Numerical relativity versus post-Minkowskian gravity, *Phys. Rev. D* **108**, 124016 (2023).
- [94] Zvi Bern, Clifford Cheung, Radu Roiban, Chia-Hsien Shen, Mikhail P. Solon, and Mao Zeng, Scattering amplitudes and the conservative hamiltonian for binary systems at third post-Minkowskian order, *Phys. Rev. Lett.* **122**, 201603 (2019).
- [95] Gregor Kälin, Zhengwen Liu, and Rafael A. Porto, Conservative dynamics of binary systems to third post-Minkowskian order from the effective field theory approach, *Phys. Rev. Lett.* **125**, 261103 (2020).
- [96] N. Emil J. Bjerrum-Bohr, Poul H. Damgaard, Ludovic Planté, and Pierre Vanhove, The amplitude for classical gravitational scattering at third Post-Minkowskian order, *J. High Energy Phys.* **08** (2021) 172.
- [97] Zvi Bern, Julio Parra-Martinez, Radu Roiban, Michael S. Ruf, Chia-Hsien Shen, Mikhail P. Solon, and Mao Zeng, Scattering amplitudes, the tail effect, and conservative binary dynamics at  $\mathcal{O}(G^4)$ , *Phys. Rev. Lett.* **128**, 161103 (2022).
- [98] Christoph Dlapa, Gregor Kälin, Zhengwen Liu, and Rafael A. Porto, Conservative dynamics of binary systems at fourth post-Minkowskian order in the large-eccentricity expansion, *Phys. Rev. Lett.* **128**, 161104 (2022).
- [99] Thibault Damour, Radiative contribution to classical gravitational scattering at the third order in  $G$ , *Phys. Rev. D* **102**, 124008 (2020).
- [100] Paolo Di Vecchia, Carlo Heissenberg, Rodolfo Russo, and Gabriele Veneziano, Radiation reaction from soft theorems, *Phys. Lett. B* **818**, 136379 (2021).
- [101] Gihyuk Cho, Gregor Kälin, and Rafael A. Porto, From boundary data to bound states. Part III. Radiative effects, *J. High Energy Phys.* **04** (2022) 154; **07** (2022) 2.
- [102] Paolo Di Vecchia, Carlo Heissenberg, Rodolfo Russo, and Gabriele Veneziano, The eikonal approach to gravitational scattering and radiation at  $\mathcal{O}(G^3)$ , *J. High Energy Phys.* **07** (2021) 169.
- [103] Enrico Herrmann, Julio Parra-Martinez, Michael S. Ruf, and Mao Zeng, Radiative classical gravitational observables at  $\mathcal{O}(G^3)$  from scattering amplitudes, *J. High Energy Phys.* **10** (2021) 148.
- [104] Donato Bini, Thibault Damour, and Andrea Geralico, Radiative contributions to gravitational scattering, *Phys. Rev. D* **104**, 084031 (2021).
- [105] Donato Bini and Andrea Geralico, Higher-order tail contributions to the energy and angular momentum fluxes in a two-body scattering process, *Phys. Rev. D* **104**, 104020 (2021).
- [106] Aneesh V. Manohar, Alexander K. Ridgway, and Chia-Hsien Shen, Radiated angular momentum and dissipative effects in classical scattering, *Phys. Rev. Lett.* **129**, 121601 (2022).
- [107] Christoph Dlapa, Gregor Kälin, Zhengwen Liu, Jakob Neef, and Rafael A. Porto, Radiation reaction and gravitational waves at fourth post-Minkowskian order, *Phys. Rev. Lett.* **130**, 101401 (2023).
- [108] Deborah Ferguson *et al.*, Second MAYA catalog of binary black hole numerical relativity waveforms, [arXiv:2309.00262](https://arxiv.org/abs/2309.00262).
- [109] Deborah Ferguson *et al.*, Mayawaves: Python library for interacting with the Einstein toolkit and the MAYA catalog, [arXiv:2309.00653](https://arxiv.org/abs/2309.00653).
- [110] Gregorio Carullo, Simone Albanesi, Alessandro Nagar, Rossella Gamba, Sebastiano Bernuzzi, Tomas Andrade, and Juan Trenado, Unveiling the merger structure of black hole binaries in generic planar orbits, *Phys. Rev. Lett.* **132**, 101401 (2024).
- [111] L. Pekowsky, R. O’Shaughnessy, J. Healy, and D. Shoemaker, Comparing gravitational waves from non-precessing and precessing black hole binaries in the corotating frame, *Phys. Rev. D* **88**, 024040 (2013).
- [112] Evan Ochsner and Richard O’Shaughnessy, Asymptotic frame selection for binary black hole spacetimes II: Post-Newtonian limit, *Phys. Rev. D* **86**, 104037 (2012).
- [113] Alessandro Nagar, Rossella Gamba, Piero Retegno, Veronica Fantini, and Sebastiano Bernuzzi, Effective-one-body waveform model for non-circularized, planar, coalescing black hole binaries: The importance of radiation reaction, [arXiv:2404.05288](https://arxiv.org/abs/2404.05288).
- [114] Donato Bini, Thibault Damour, and Andrea Geralico, Novel approach to binary dynamics: Application to the fifth post-Newtonian level, *Phys. Rev. Lett.* **123**, 231104 (2019).

- [115] Thibault Damour and Alessandro Nagar, New effective-one-body description of coalescing nonprecessing spinning black-hole binaries, *Phys. Rev. D* **90**, 044018 (2014).
- [116] Alessandro Nagar *et al.*, Time-domain effective-one-body gravitational waveforms for coalescing compact binaries with nonprecessing spins, tides and self-spin effects, *Phys. Rev. D* **98**, 104052 (2018).
- [117] Tomas Andrade *et al.*, Towards numerical-relativity informed effective-one-body waveforms for dynamical capture black hole binaries, *Phys. Rev. D* **109**, 084025 (2024).
- [118] Simone Albanesi, Alessandro Nagar, and Sebastiano Bernuzzi, Effective one-body model for extreme-mass-ratio spinning binaries on eccentric equatorial orbits: Testing radiation reaction and waveform, *Phys. Rev. D* **104**, 024067 (2021).
- [119] Alessandro Nagar and Piero Retegno, Efficient effective one body time-domain gravitational waveforms, *Phys. Rev. D* **99**, 021501 (2019).
- [120] Rossella Gamba, Sebastiano Bernuzzi, and Alessandro Nagar, Fast, faithful, frequency-domain effective-one-body waveforms for compact binary coalescences, *Phys. Rev. D* **104**, 084058 (2021).
- [121] Md Arif Shaikh, Vijay Varma, Harald P. Pfeiffer, Antoni Ramos-Buades, and Maarten van de Meent, Defining eccentricity for gravitational wave astronomy, *Phys. Rev. D* **108**, 104007 (2023).
- [122] Jeremy D. Schnittman, Spin-orbit resonance and the evolution of compact binary systems, *Phys. Rev. D* **70**, 124020 (2004).
- [123] Rossella Gamba *et al.*, Highly accurate simulations of eccentric, non-planar binary black holes systems.
- [124] Ian Harry, Stephen Privitera, Alejandro Bohé, and Alessandra Buonanno, Searching for gravitational waves from compact binaries with precessing spins, *Phys. Rev. D* **94**, 024012 (2016).
- [125] Ian Harry, Juan Calderón Bustillo, and Alex Nitz, Searching for the full symphony of black hole binary mergers, *Phys. Rev. D* **97**, 023004 (2018).
- [126] D. Shoemaker, Advanced LIGO anticipated sensitivity curves OBSOLETE, Report No. LIGO Document T0900288-v3, <https://dcc.ligo.org/cgi-bin/DocDB/ShowDocument?docid=2974>.
- [127] Jake Mac Uilliam, Sarp Akcay, and Jonathan E. Thompson, A survey of four precessing waveform models for binary black hole systems, *Phys. Rev. D* **109**, 084077 (2024).
- [128] <https://bitbucket.org/teobresums/teobresums/src/GIOTTO/>.
- [129] Raoul-Martin Memmesheimer, Achamveedu Gopakumar, and Gerhard Schaefer, Third post-Newtonian accurate generalized quasi-Keplerian parametrization for compact binaries in eccentric orbits, *Phys. Rev. D* **70**, 104011 (2004).